



THE UNIVERSITY *of* EDINBURGH

Edinburgh Research Explorer

A numerical study of the settling of non-spherical particles in quiescent water

Citation for published version:

Cheng, X, Cao, Z, Li, J & Borthwick, A 2023, 'A numerical study of the settling of non-spherical particles in quiescent water', *Physics of Fluids*, vol. 35, 093310. <https://doi.org/10.1063/5.0165555>

Digital Object Identifier (DOI):

[10.1063/5.0165555](https://doi.org/10.1063/5.0165555)

Link:

[Link to publication record in Edinburgh Research Explorer](#)

Document Version:

Peer reviewed version

Published In:

Physics of Fluids

General rights

Copyright for the publications made accessible via the Edinburgh Research Explorer is retained by the author(s) and / or other copyright owners and it is a condition of accessing these publications that users recognise and abide by the legal requirements associated with these rights.

Take down policy

The University of Edinburgh has made every reasonable effort to ensure that Edinburgh Research Explorer content complies with UK legislation. If you believe that the public display of this file breaches copyright please contact openaccess@ed.ac.uk providing details, and we will remove access to the work immediately and investigate your claim.



1 **A numerical study of the settling of non-spherical particles in quiescent water**

2 Xiaoyong Cheng (程潇勇)¹, Zhixian Cao (曹志先)^{1,a)}, Ji Li (李季)², Alistair Borthwick^{3,4}

3

4 AFFILIATIONS

5 ¹State Key Laboratory of Water Resources Engineering and Management, Wuhan
6 University, Wuhan 430072, China

7 ²Zienkiewicz Centre for Computational Engineering, Faculty of Science and Engineering,
8 Swansea University, Swansea SA1 8EN, UK

9 ³Institute for Infrastructure and Environment, The University of Edinburgh, Edinburgh
10 EH9 3JL, UK

11 ⁴School of Engineering, Computing and Mathematics, University of Plymouth, Plymouth
12 PL4 8AA, UK

13

14 ^{a)}Author to whom correspondence should be addressed: zxcao@whu.edu.cn

15

16 ABSTRACT

17 The settling of non-spherical particles is poorly understood, with previous studies
18 having focused mainly on spherical particles. Here, a series of particle-resolved direct
19 numerical simulations are conducted using FLOW-3D (commercial computational fluid
20 dynamics software) for spheres and five regular, non-spherical shapes of sediment
21 particles, i.e., prolate spheroid, oblate spheroid, cylinder, disk, and cube. The Galileo
22 number varies from 0.248 to 360 and the particle Reynolds number Re_p ranges from
23 0.00277 to 562. The results show that a non-spherical particle may experience larger drag
24 and consequently attain a lower terminal velocity than an equivalent sphere. If Re_p is
25 sufficiently small, the terminal velocity is less affected by particle shape as characterized
26 by the particle aspect ratio. For relatively large Re_p , the shape effect (represented by the
27 Corey shape factor) becomes more significant. Empirical correlations are derived for the
28 dimensionless characteristic time t_{95^*} and displacement s_{95^*} of particle settling, which
29 show that t_{95^*} remains constant in the Stokes regime ($Re_p < 1$) and decreases with
30 increasing Re_p in the intermediate regime ($1 \leq Re_p < 10^3$), whereas s_{95^*} increases
31 progressively with increasing Re_p over the simulated range. It is also found that in the
32 Stokes regime, particle orientation remains essentially unchanged during settling, and so
33 the terminal velocity is governed by the initial orientation. In the intermediate regime, a
34 particle provisionally settling at an unstable orientation self-readjusts to a stable
35 equilibrium state, such that the effect of initial orientation on the terminal velocity is
36 negligible. Moreover, an unstable initial orientation can enhance the vertical displacement
37 and may promote vortex shedding.

38

39 HIGHLIGHTS

- 40 ● Settling of non-spherical particles is investigated using commercial computational
41 fluid dynamics software.
- 42 ● At low particle Reynolds numbers, an increase in particle aspect ratio may
43 correspond to a reduction in terminal velocity.
- 44 ● The characteristic time remains constant throughout the Stokes regime and decreases
45 with increasing particle Reynolds number in the intermediate regime.
- 46 ● An unstable initial orientation may promote vortex shedding from particles settling
47 in the intermediate regime.
- 48

49 I. INTRODUCTION

50 The settling of particles in fluids is key to many natural and industrial processes,
51 such as sediment dynamics in alluvial rivers,^{1,2} transportation of marine microplastics,^{3,4}
52 proppant settling in hydraulic fractures,^{5,6} and chemical and powder processing.⁷
53 Although particulate flows are generally turbulent and involve large amounts of particles,
54 an improved understanding of the settling of a single particle in quiescent fluid is a
55 prerequisite for modelling complex particle-laden turbulent flows. However, most
56 existing models of particulate flows assume the grains to be spheres when in fact the most
57 commonly encountered particles in practical applications are non-spherical.^{8,9} Such
58 simplification inevitably ignores the key roles played by particle shape and orientation in
59 the settling process. Studies are urgently needed to gain better insight into the settling of
60 non-spherical particles in quiescent water.

61 When a heavy particle falls through a static fluid, the particle accelerates due to
62 gravity and increasing fluid drag is exerted on its surface. As the submerged weight of the
63 particle is balanced by fluid drag, its acceleration terminates, enabling the particle to fall
64 at a nearly constant velocity, called the terminal velocity. The drag force is one of the
65 fundamental forces that affect the settling process, which can be defined as

$$66 \quad F_d = \frac{1}{2} C_d \rho_f W^2 \frac{\pi}{4} d_n^2, \quad (1)$$

67 where C_d is the drag coefficient; ρ_f is the fluid density; W is the settling velocity;
68 and d_n is the diameter of a sphere of equivalent volume to that of the particle. Accurate
69 estimates of settling velocity and drag coefficient are of particular importance because
70 other parameters can be readily inferred. Notably, the terminal velocity of a particle,
71 denoted W_t , can be simply derived by equating the drag force to the submerged weight

72 of the particle. The drag coefficient C_d in Eq. (1) is however very challenging to
73 determine because it depends on many parameters including the particle Reynolds
74 number and particle shape.¹⁰ Herein, the particle Reynolds number is defined as
75 $Re_p = Wd_n / \nu$, with ν being the kinematic viscosity. Except at sufficiently small Re_p ,
76 where an analytical solution exists for spheres based on Stokes' law, in which C_d is
77 inversely proportional to Re_p , no general solution can be found for determining the drag
78 coefficient of particles of any shape. Based on a large number of theoretical and
79 experimental investigations of settling behavior, numerous empirical models have been
80 developed to predict the drag coefficient and settling velocity of spherical particles¹¹⁻¹³
81 and non-spherical particles.¹⁴⁻¹⁸ To account for the shape effect of non-spherical particles,
82 various approaches have been proposed to define particle shape. Of these, the Corey shape
83 factor¹⁹ (CSF) is the most commonly used shape descriptor,^{14,20,21} and is defined as
84 $CSF = d_s / \sqrt{d_m d_l}$, where d_s , d_m , and d_l are respectively the shortest, intermediate,
85 and longest form dimensions of the particle. Sphericity ϕ is another widely used shape
86 descriptor,^{15,22,23} and is given by the ratio of the surface area of the volume-equivalent
87 sphere to that of the actual particle. Circularity X is the ratio of the perimeter of the
88 maximum projection area of the particle to the perimeter of a circle that has area equal to
89 the maximum projection area. This descriptor is able to reflect the irregularity of particle
90 contours and is thus very suitable for particles with sharp corners and large obtuse
91 angles.²⁴ In addition, for highly irregular particles, the parameter ξ , which is the ratio
92 ϕ / X , is another effective shape descriptor.^{17,25,26} However, these aforementioned
93 empirical models cannot provide sufficient effective information to quantify the whole
94 process of particle settling. Consequently, the time and space scales that are required for

95 a particle to reach its terminal settling state have not yet been resolved.

96 Particle orientation also has a vital effect on settling non-spherical particles. In
97 general, a non-spherical particle could fall at any orientation without rotation at
98 sufficiently small Re_p ,^{27,28} but will assume a stable orientation and tend to fall with the
99 maximum projection area normal to the direction of settling motion at relatively large
100 Re_p .^{8,29} Besides, particle orientation can appreciably modify the drag coefficient.^{16,18}
101 Over the past decade, particle-resolved direct numerical simulation (PR-DNS) has been
102 carried out to establish correlations between C_d and particle orientation.³⁰⁻³³ However,
103 such correlations are based on the assumption of a stationary obstacle exposed to a
104 moving fluid, therefore neglecting the effects of secondary motions and wake structures.³⁴
105 Moreover, most existing numerical studies considering the influence of particle
106 orientation on free settling have been confined to two-dimensional modeling.³⁵⁻³⁷ Overall,
107 there is a need for a three-dimensional model that can properly address the effect of
108 particle orientation on the settling process of non-spherical particles.

109 The present work sets out to unravel the effects of particle shape and initial
110 orientation on the settling of non-spherical sediment particles in quiescent water. Using
111 the commercial computational fluid dynamics (CFD) software FLOW-3D (version 11.2),
112 a series of PR-DNS simulations are performed for a range of particle sizes, shapes, and
113 distinct initial orientations. Based on the computational results, key parameters that
114 characterize the settling process, including terminal velocity W_t and drag coefficient
115 C_d , are analyzed to reveal the influence of particle shape on settling. Furthermore, the
116 time and space scales required to reach terminal settling are also investigated. In addition,
117 the settling processes of non-spherical particles in the Stokes and intermediate regimes
118 are presented, thereby probing into the effect of initial particle orientation.

119 II. METHOD

120 A. Computational fluid dynamics (CFD) model

121 The commercial CFD software FLOW-3D, developed by Flow Science, is used to
122 conduct PR-DNS simulations of particle settling in otherwise quiescent fluid. FLOW-3D
123 utilizes a fractional area/volume obstacle representation (FAVOR) technique³⁸ and
124 provides a general moving object model that can simulate rigid body motion that is
125 dynamically coupled with fluid flow. The FAVOR method defines complicated geometric
126 shapes through fractional areas and volumes within rectangular elements and has proven
127 to be one of the most efficient methods to treat immersed solid bodies.^{39,40}

128 Assuming the fluid to be incompressible, the continuity and momentum equations
129 based on the FAVOR method are given as

$$130 \quad \frac{\partial U_i}{\partial x_i} = -\frac{\partial V_f}{\partial t}, \quad (2)$$

$$131 \quad \frac{\partial u_i}{\partial t} + \frac{U_j}{V_f} \frac{\partial u_i}{\partial x_j} = -\frac{1}{\rho_f} \frac{\partial p}{\partial x_i} + g_i + f_i, \quad (3)$$

132 where subscripts i and $j=1,2,3$ denote x , y , and z directions; x_i are Cartesian
133 coordinates; t is time; $U_i = u_i A_i = (uA_x, vA_y, wA_z)$ in which u_i is the i -th velocity
134 component and A_i is the corresponding area fraction; V_f is volume fraction; p is
135 pressure; g_i is the i -th body acceleration component; and f_i is the i -th viscous
136 acceleration component. The viscous acceleration components in Eq. (3) are calculated
137 as

$$138 \quad f_i = \frac{1}{\rho_f V_f} \left(\omega s x_i - \frac{\partial T_{ij}}{\partial x_j} \right), \quad (4)$$

139 where w_{sx_i} are wall shear stress components; and $T_{ij} = A_j \tau_{ij} = -2A_j \mu (s_{ij} - s_{kk} \delta_{ij} / 3)$, in
 140 which μ is dynamic viscosity, $s_{ij} = (\partial u_i / \partial x_j + \partial u_j / \partial x_i) / 2$ is the strain rate tensor,
 141 and δ_{ij} is the Kronecker delta function. Compared to the continuity equation applied in
 142 stationary obstacle problems, $-\partial V_f / \partial t$ on the right-hand side of Eq. (2) is equivalent to
 143 an additional volume source term and exists solely in mesh cells around the boundary of
 144 the moving object. The term is evaluated as

$$145 \quad -\frac{\partial V_f}{\partial t} = \frac{S_{\text{obj}}}{V_{\text{cell}}} V_{\text{obj}i} n_i, \quad (5)$$

146 where V_{cell} is the volume of a mesh cell; S_{obj} , n_i , and $V_{\text{obj}i}$ are respectively the
 147 surface area, unit normal vector, and velocity of the moving object in the mesh cell.

148 According to kinematics, the general motion of a rigid body can be divided into
 149 translational motion and rotational motion components. Newton's second law describes
 150 the translational motion of a rigid body as

$$151 \quad m_p \frac{d\mathbf{V}_G}{dt} = \mathbf{F}, \quad (6)$$

152 where \mathbf{V}_G is the mass center velocity of the rigid body; \mathbf{F} is the total force on the body;
 153 and m_p is rigid body mass. Euler's equation describes rigid body rotation in a frame of
 154 reference fixed at the centroid of the rotating body as

$$155 \quad \mathbf{I} \frac{d\boldsymbol{\omega}}{dt} + \boldsymbol{\omega} \times (\mathbf{I}\boldsymbol{\omega}) = \mathbf{T}_G, \quad (7)$$

156 where $\boldsymbol{\omega}$ is the angular velocity of the rigid body; \mathbf{I} is the diagonal inertia matrix
 157 relative to the principal axes of the rigid body; and \mathbf{T}_G is the total torque about the mass
 158 center. The present paper considers the free settling of a single particle, so the total force
 159 and total torque include only hydrodynamic and gravitational forces and torques.

160 The CFD model solves the governing equations of fluid motion [Eqs. (2) and (3)]
 161 using a finite volume/finite difference method.⁴¹ Pressures and velocities are coupled
 162 implicitly and solved by using a generalized minimal residual method, which is the
 163 default solver of FLOW-3D. The momentum advection algorithm adopts a first-order
 164 upwind scheme. For coupled rigid body motion [Eqs. (6) and (7)], both the explicit and
 165 implicit general moving objects methods work well since heavy object problems are
 166 considered in the present paper.

167

168 B. Study cases

169 A series of numerical cases are used to investigate the influences of particle shape
 170 and initial orientation on the settling of non-spherical particles. Table I summarizes the
 171 simulation parameters. In all cases, the fluid is specified as water at 20 °C ($\rho_f = 1000$
 172 kg/m³, $\nu = 1 \times 10^{-6}$ m²/s), and the particles are assumed to be composed of siliciclastic
 173 sediment of homogeneous density 2650 kg/m³. Eight spherical equivalent diameters are
 174 considered, i.e., $d_n = 0.015625, 0.03125, 0.0625, 0.125, 0.25, 0.5, 1, \text{ and } 2$ mm.
 175 Consequently, the value of the Galileo number varies from 0.248 to 360. The Galileo
 176 number Ga is the ratio between gravitational and viscous forces, and is defined as

$$177 \quad Ga = \frac{\sqrt{|\rho_p / \rho_f - 1|} g d_n^3}{\nu}, \quad (8)$$

178 where ρ_p is particle density; and g is gravitational acceleration. As indicated in Table
 179 II, six particle shapes are considered, including spheres and five regular non-spherical
 180 shapes, i.e., prolate spheroid, oblate spheroid, cylinder, disk, and cube, with the first four
 181 shapes being axisymmetric. Although particles in natural and industrial processes are
 182 generally irregular, it is justified to choose regular non-spherical particles as the object of

183 the present study because most accurate models for predicting the behavior of non-
184 spherical particles in fluids have been based on studies on regular particles, for which the
185 characterization of the particle shape is not complex.¹⁸

186 Among the parameters listed in Table I, β is defined as the angle between the plane
187 in which the maximum projection area of a particle lies and the horizontal plane
188 perpendicular to the direction of settling motion (and thus provides a reasonable
189 description of the particle orientation). β_0 denotes the initial orientation of a particle
190 upon release. As previously noted, a particle settling at sufficiently small Re_p exhibits
191 no preferred orientation. If Re_p is relatively large, a particle tends to fall with its
192 maximum projection area normal to the direction of settling motion, i.e., at a state of
193 $\beta = 0^\circ$. Therefore, the typical initial state of $\beta_0 = 0^\circ$ is chosen to exclude any influence
194 of orientation variation; the combination of different particle sizes and shapes leads to 36
195 cases. A further 32 cases that consider two distinct initial orientations ($\beta_0 = 45^\circ$ and 90°)
196 are simulated for axisymmetric particles with four selected spherical equivalent diameters
197 ($d_n = 0.015625, 0.0625, 0.25,$ and 1 mm). Overall, a total of 68 numerical cases are
198 considered, and the particle Reynolds number Re_p ranges from 0.00277 to 562,
199 covering both the Stokes regime ($Re_p < 1$) and the intermediate regime ($1 \leq Re_p < 10^3$).

200 In this paper, the Corey shape factor CSF is used to describe particle shape, noting
201 that CSF suffices for regular particles.⁴² The projection area protocol, which is associated
202 with the lowest operator-dependent errors compared to other methods,⁴³ is applied to
203 determine the form dimensions of a given particle (see Table II). Particle settling is
204 simulated in a domain of dimensions $8d_n \times 8d_n$ in the x and y directions. The size of the
205 domain in the z -direction is carefully determined to ensure the whole-process modeling

206 of particle settling can be achieved without exceptional computational cost. A resolution
207 of 12 grids per d_n is used, which can successfully resolve the geometry of both spherical
208 and non-spherical particles considered in the present study. Periodic boundary conditions
209 are imposed in the horizontal directions to mimic an unbounded domain without wall
210 effect, and a free surface and a stationary wall are implemented at the upper and bottom
211 boundaries. More information on validation of the CFD model is given in the Appendix.
212 In addition, a dual-Euler whole-attitude solver is used to reproduce the variation in
213 orientation of particles, based on the time series of particle angular velocities output from
214 the CFD model. A brief description of the method is given in the Supplementary Material.
215

216

217 **TABLE I.** Summary of simulation parameters.

ρ_f (kg/m ³)	ν (m ² /s)	ρ_p (kg/m ³)	d_n (mm)	β_0 (°)
1000	1×10^{-6}	2650	0.015625-2	0, 45 and 90

218

219 **TABLE II.** Summary of six particle shapes considered in this work. Semi-axes lengths
 220 of the ellipsoid are a , b , and c ; the diameter and height of the cylinder and disk are d
 221 and h ($d < h$ for the cylinder, $d > h$ for the disk), respectively; and the edge length of
 222 the cube is a .

Shape	d_l	d_m	d_s	CSF
Sphere	d_n	d_n	d_n	1.00
Ellipsoid 1 (prolate spheroid, $a = 4b = 4c$)	$2a$	$2b$	$2c$	0.50
Ellipsoid 2 (oblate spheroid, $a = b = 2c$)	$2a$	$2b$	$2c$	0.50
Cylinder ($h = 2d$)	$\sqrt{h^2 + d^2}$	d	d	0.67
Disk ($h = 1/4d$)	$\sqrt{h^2 + d^2}$	d	h	0.25
Cube	$\sqrt{3}a$	$\sqrt{2}a$	a	0.64

223

224

225 III. RESULTS AND DISCUSSION

226 A. Particle settling with maximum projection area normal to fall direction

227 1. Terminal settling state

228 The terminal settling state and terminal velocity of a particle are simultaneously
 229 attained when the submerged weight of the particle is balanced by fluid drag. Terminal
 230 velocity is a fundamental hydrodynamic parameter that both directly and indirectly
 231 governs sedimentary processes.²⁹ Here, the terminal velocity W_t and spherical
 232 equivalent diameter d_n are normalized following Dietrich¹⁴, such that:

$$233 \quad W_{t*} = \frac{\rho_f W_t^3}{(\rho_s - \rho_f) g V}, \quad (9)$$

$$234 \quad d_* = \frac{(\rho_s - \rho_f) g d_n^3}{\rho_f V^2}, \quad (10)$$

235 where W_{t*} is the dimensionless terminal velocity; and d_* is the dimensionless
 236 spherical equivalent diameter. Figure 1 illustrates the variation in W_{t*} with d_* obtained
 237 for different shapes when $\beta_0 = 0^\circ$. It appears that a non-spherical particle attains a lower
 238 terminal velocity than its spherical counterpart, with the difference in terminal velocity
 239 becoming increasingly evident as the particle size increases. This trend is further
 240 confirmed in Figure 2 which shows the variation in δ with particle Reynolds number
 241 Re_p where δ is defined as the relative deviation of the terminal velocity of a non-
 242 spherical particle from that of its spherical counterpart with the same d_n as follows:

$$243 \quad \delta = \frac{W_t - W_{t\text{-sphere}}}{W_{t\text{-sphere}}} \times 100\%. \quad (11)$$

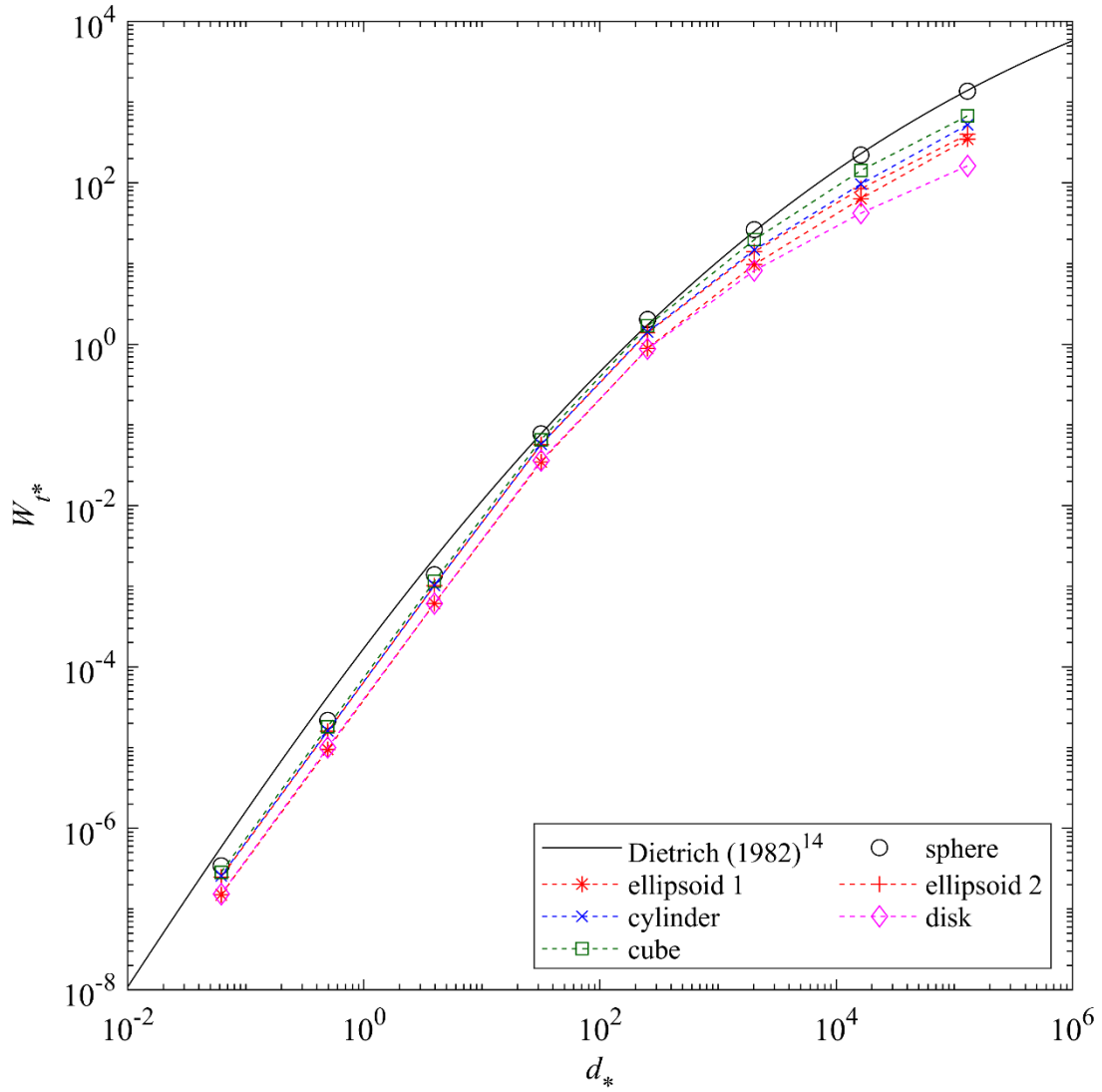
244 For a specific non-spherical particle shape, δ remains essentially unchanged in the

245 Stokes regime, whereas δ decreases progressively with increasing Re_p in the
246 intermediate regime. Fig. 2 also shows that δ varies with particle shape. In addition to
247 the CSF, the aspect ratio obtained by dividing d_l by d_s is selected here to account
248 for the shape effect. In the Stokes regime with low Re_p , δ is largely dependent on
249 aspect ratio, with larger particle aspect ratio corresponding to smaller terminal velocity.
250 The foregoing observations indicate that the longest and shortest form dimensions may
251 govern terminal velocity in the Stokes regime. Therefore, elongated, flat particles may
252 reach almost equal values of terminal velocity despite their distinct shapes. When Re_p
253 exceeds 10, the computed δ generally decreases with decreasing CSF, and little
254 consistency is observed between δ and the aspect ratio. In short, when the viscous force
255 dominates, the terminal velocity is less affected by the non-spherical particle shape, which
256 can be characterized by the particle aspect ratio. When the inertial force becomes
257 dominant, the shape effect tends to become significant, and should be represented by
258 CSF instead of aspect ratio.

259 Figure 3 illustrates the drag coefficient C_d as a function of particle Reynolds
260 number Re_p . Results obtained from the spherical drag law proposed by Clift and
261 Gauvin¹¹ are also included for comparison. The computed C_d curve for spheres exhibits
262 satisfactory agreement with Clift and Gauvin's empirical relationship, confirming the
263 validity of the present model. Non-spherical particles are predicted to experience
264 relatively larger drag than equivalent spheres, with the difference between drag
265 coefficient values progressively increasing as Re_p increases.

266 When a particle moves through a fluid, the total drag exerted on its surface can be
267 divided into pressure drag (or form drag) F_{pd} and friction drag F_{fd} . We consider the

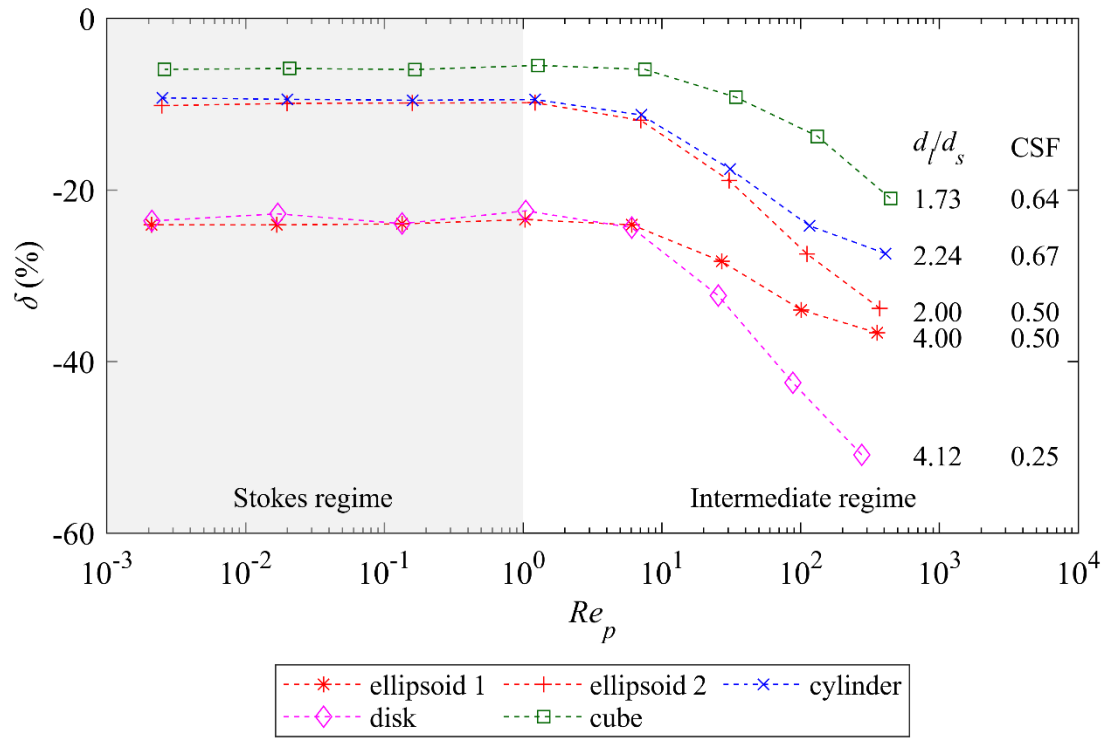
268 drag ratio F_{fd} / F_{pd} which is defined as the ratio between friction drag and pressure drag
269 of a particle at the terminal settling state. Figure 4 illustrates the dependency of the drag
270 ratio F_{fd} / F_{pd} on particle Reynolds number Re_p . The computed F_{fd} / F_{pd} of spheres
271 settling in the Stokes regime is approximately 2, close to the theoretically derived value.²
272 Moreover, the computed F_{fd} / F_{pd} of a specific shape remains constant throughout the
273 Stokes regime and gradually decreases as Re_p increases in the intermediate regime. For
274 given Re_p , the value of F_{fd} / F_{pd} generally increases with increasing CSF. These
275 results suggest that when the inertial force becomes significant or the particle shape
276 deviates from spherical, pressure drag gradually dominates over friction drag.
277



278

279 **FIG. 1.** Dimensionless terminal velocity W_{t*} against dimensionless spherical equivalent
 280 diameter d_* obtained for different particle shapes when $\beta_0 = 0^\circ$. Solid line refers to the
 281 model by Dietrich¹⁴.

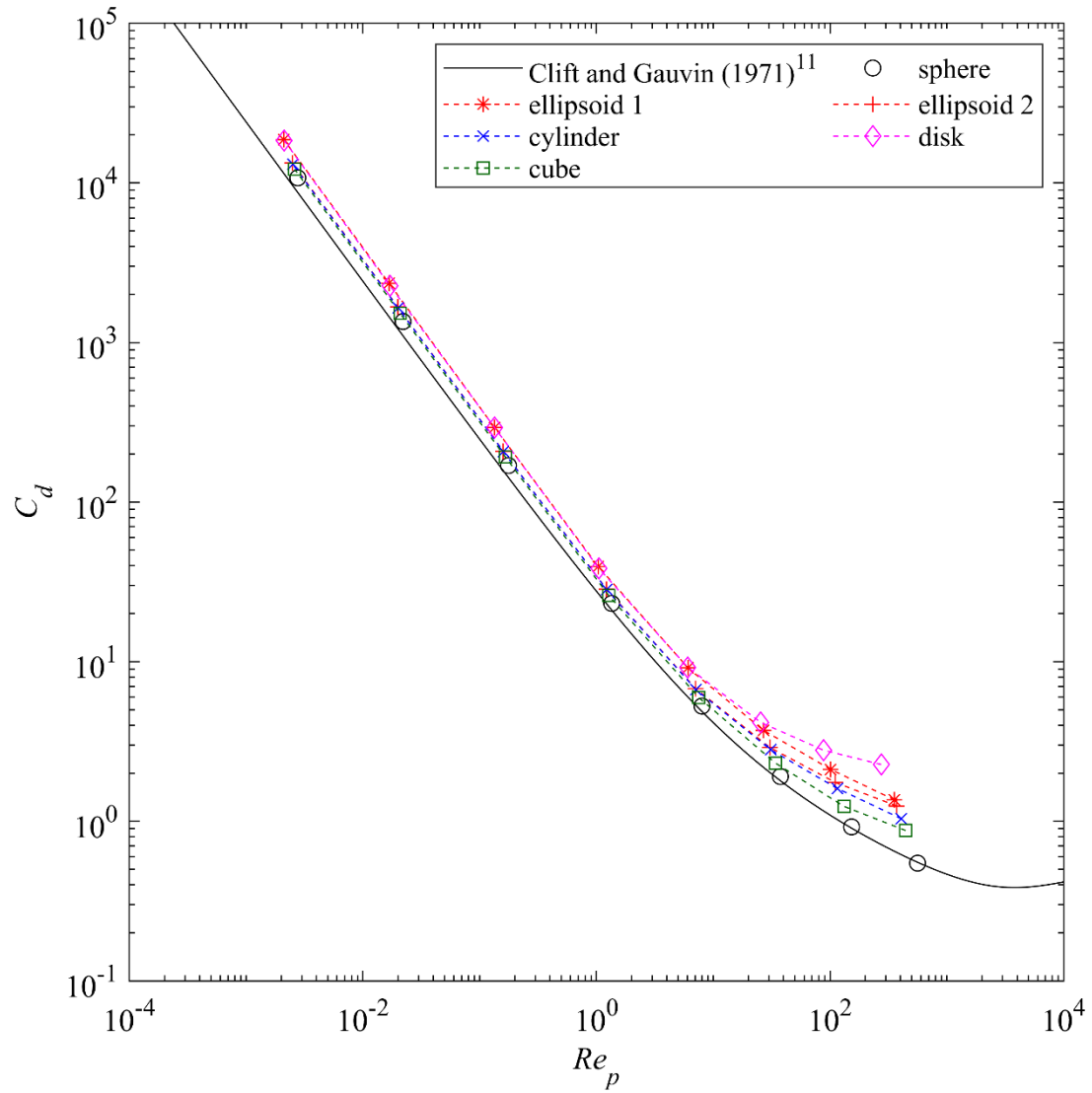
282



283

284 **FIG. 2.** Predicted dependence of relative deviation δ in terminal velocity of a non-
 285 spherical particle to that of a sphere of the same equivalent diameter on particle Reynolds
 286 number Re_p .

287



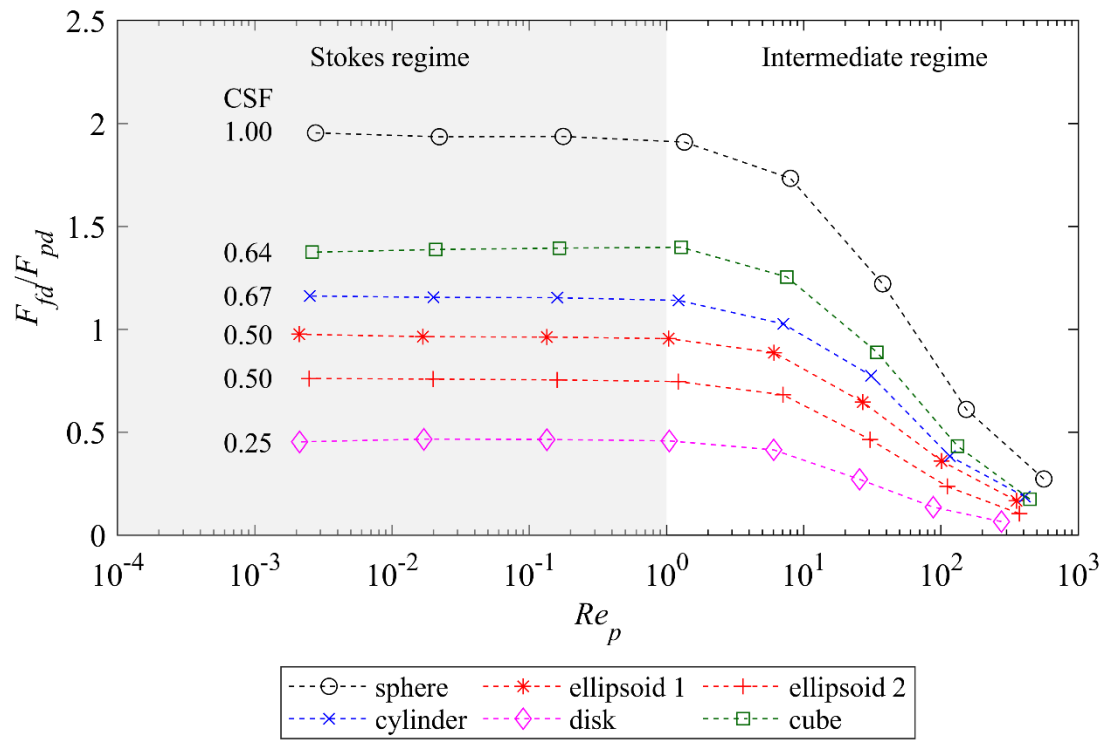
288

289 **FIG. 3.** Dependence of predicted drag coefficient C_d on particle Reynolds number Re_p .

290 Solid line is the spherical drag law proposed by Clift and Gauvin¹¹.

291

292



293

294 **FIG. 4.** Predicted dependence of drag ratio F_{fd} / F_{pd} on particle Reynolds number Re_p .

295

296 2. *Characteristic time and displacement*

297 Although the settling velocity and drag coefficient have been extensively studied for
298 both spherical and non-spherical particles, limited attention has been paid to the time and
299 space scales required for a particle to reach its terminal settling state.

300 The motion of a spherical particle falling through a fluid is described theoretically
301 by the Boussinesq-Basset-Oseen equation,² expressed as

$$302 \quad (m_p + \alpha_m m_f) \frac{dW}{dt} = (m_p - m_f)g - F_d - \frac{3}{2} d_n^2 (\pi \rho_f \mu)^{1/2} \int_0^t \frac{dW}{d\sigma} \frac{d\sigma}{(t - \sigma)^{1/2}}, \quad (12)$$

303 where m_f is the mass of fluid displaced by the sphere; α_m is the added mass coefficient;
304 and σ is a dummy variable. In Eq. (12), the term on the left-hand side denotes particle
305 inertia, and includes the added mass effect when an accelerating (or retarding) particle
306 moves in a fluid. In practice, it is common to assume $\alpha_m = 0.5$. On the right-hand side
307 of Eq. (12), the first term is the submerged weight of the particle, the second term
308 represents the fluid drag, and the third term is the Basset force (due to particle acceleration
309 because of unsteady viscous shear on the surface of the particle).

310 Guo⁴⁴ derived a simple closed-form solution for the motion of a sphere settling
311 through a fluid by applying Rubey's drag law⁴⁵ to Eq. (12) and combining the added mass
312 and the Basset force into an integrated term. Guo was able to determine analytically the
313 time-dependent settling velocity, acceleration, and vertical displacement of a spherical
314 particle. However, for a non-spherical particle, even when the orientation variation is
315 neglected and the drag force approximated by an empirical relationship, it is extremely
316 difficult to obtain analytical solutions for the added mass and the Basset force. In practice,
317 empirical relations have to be introduced in order to describe the characteristic time and
318 characteristic displacement of a settling non-spherical particle.

319 Here, we focus on cases with $\beta_0 = 0^\circ$, where particles accelerate to the terminal
 320 settling state with negligible change in orientation. The characteristic time t_{95} and
 321 characteristic displacement s_{95} are defined as the time and vertical displacement taken
 322 for a particle to reach 95% of its terminal velocity. A general dimensional analysis gives
 323 the following expressions:

$$324 \quad t_{95*} = \frac{t_{95}}{d_n^2 / \nu} = f_1(Re_p), \quad (13)$$

$$325 \quad s_{95*} = \frac{s_{95}}{d_n} = f_2(Re_p), \quad (14)$$

326 where t_{95*} and s_{95*} are dimensionless characteristic time and displacement. Figure 5
 327 depicts the behavior of t_{95*} and s_{95*} with Re_p , as logarithmic plots. Linear fitting is
 328 used to obtain two asymptotes for the Stokes and intermediate regimes, with their
 329 intersection set at $Re_p = 1$. As shown in Fig. 5(a), the dimensionless characteristic time
 330 t_{95*} is assumed constant throughout much of the Stokes regime, and then decreases with
 331 increasing Re_p in the intermediate regime. The dimensionless characteristic
 332 displacement s_{95*} increases monotonically with increasing Re_p over the simulated
 333 range, with the linear slope observed in the Stokes regime reducing in the intermediate
 334 regime [Fig. 5(b)]. These results suggest that the Stokes and intermediate regimes are
 335 characterized by two distinct acceleration mechanisms. Based on the two asymptotes, the
 336 logarithmic matching approach proposed by Guo⁴⁶ is used to establish the following
 337 correlation formulae:

$$338 \quad t_{95*} = 2.226 \left(1 + Re_p^{3.126}\right)^{-0.222}, \quad (15)$$

$$339 \quad s_{95*} = 1.716 Re_p^{0.998} \left(1 + Re_p^{3.409}\right)^{-0.209}. \quad (16)$$

340 The above correlations are evaluated using the coefficient of determination R^2 and
 341 mean relative error MRE, which are defined as

$$342 \quad R^2 = 1 - \frac{\sum_{k=1}^N (\eta_k^{\text{cal}} - \eta_k^{\text{sim}})^2}{\sum_{k=1}^N (\overline{\eta^{\text{sim}}} - \eta_k^{\text{sim}})^2}, \quad (17)$$

$$343 \quad \text{MRE} = \frac{1}{N} \sum_{k=1}^N \left| \frac{\eta_k^{\text{cal}} - \eta_k^{\text{sim}}}{\eta_k^{\text{sim}}} \right|, \quad (18)$$

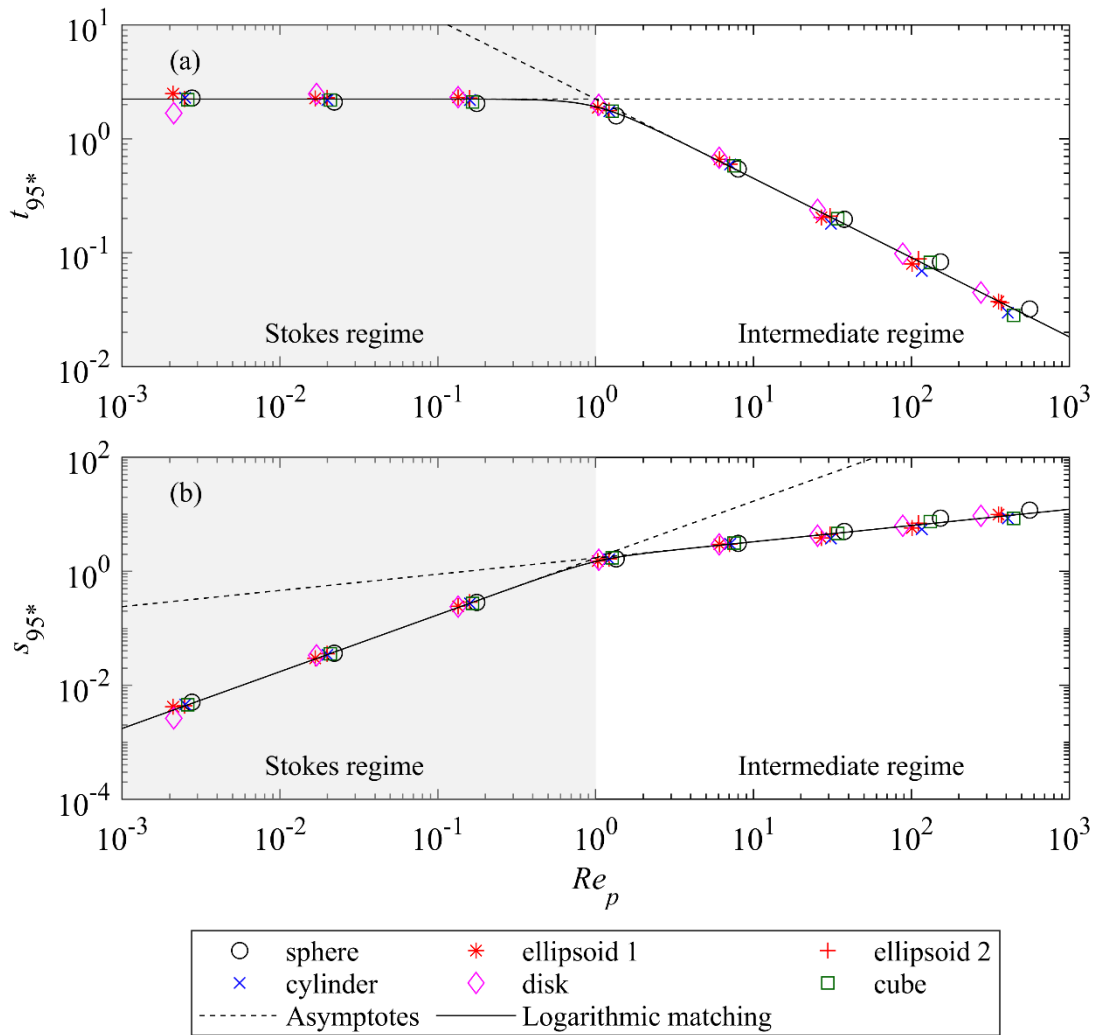
344 where η_k^{cal} is the k -th data value obtained from the correlation functions; η_k^{sim} is the k -
 345 th data value from the numerical simulations; $\overline{\eta^{\text{sim}}}$ is the mean value of the simulated
 346 data; and N is the number of pairs of data points. In general, higher R^2 and lower
 347 MRE correspond to better model performance. As demonstrated in Table III, our
 348 theoretical model exhibits rather good performance with high R^2 and acceptable
 349 MRE. The proposed correlations indicate that the time and space scales required for a
 350 non-spherical particle to reach its terminal settling state may vary with Re_p , and provide
 351 convenient methods that give effective estimates of the magnitudes of the characteristic
 352 time and displacement. It should be noted that the proposed correlations are only valid
 353 within the simulated range of Re_p for a particle-to-fluid density ratio ρ_p / ρ_f of 2.65.
 354 Future work will be extended to the Newton regime ($Re_p > 10^3$) and incorporate a larger
 355 range of density ratios.

356

357 **TABLE III.** Performance of proposed correlation formulae Eq. (15) for dimensionless
 358 characteristic time and Eq. (16) for dimensionless characteristic displacement against
 359 underlying simulated data.

Correlation	R^2	MRE (%)
Eq. (15)	0.9971	5.948
Eq. (16)	0.9988	3.453

360



362 **FIG. 5.** Dependence on particle Reynolds number Re_p of (a) dimensionless
 363 characteristic time t_{95*} and (b) dimensionless characteristic displacement s_{95*} .

364

365 B. Particle settling for different initial orientations.

366 1. *Stokes regime*

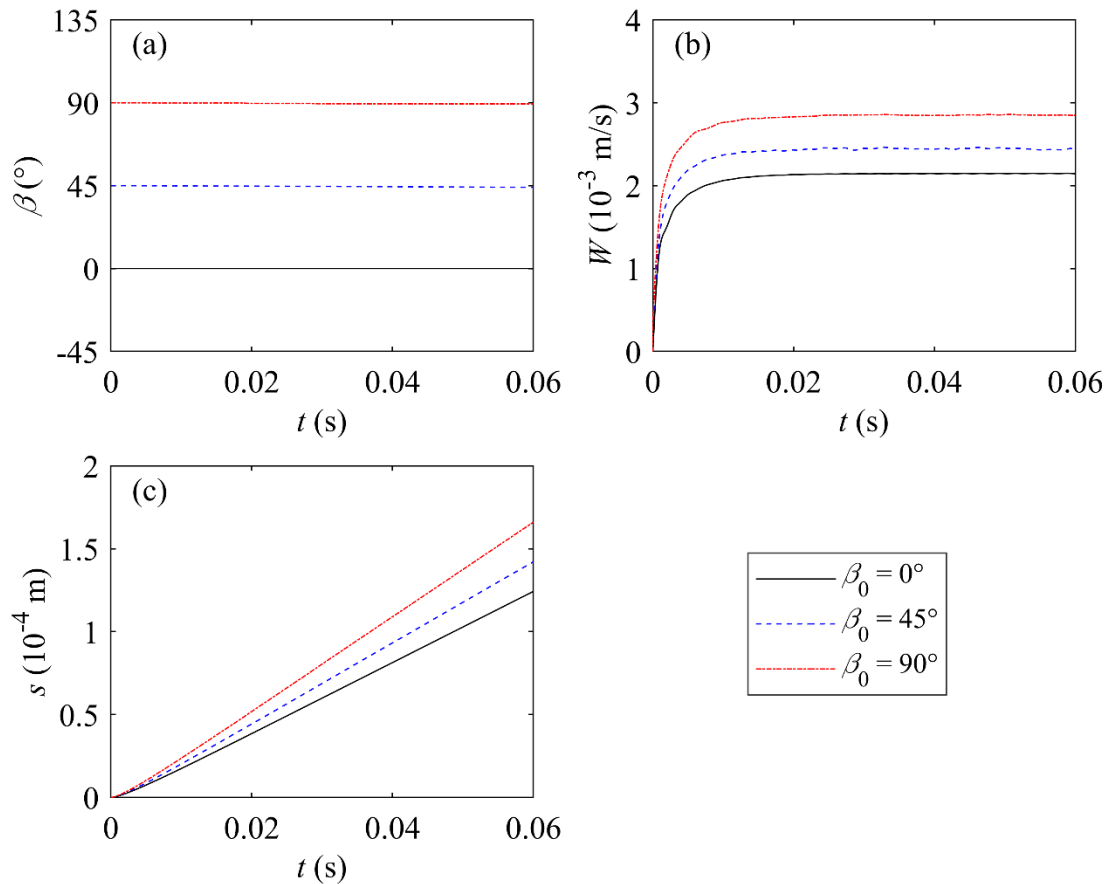
367 In this section, results from numerical cases with $d_n = 0.0625$ mm and Re_p
368 ranging from 0.1 to 0.2 are analyzed to investigate the effect of initial orientation on the
369 settling of non-spherical particles in the Stokes regime. Note that similar results are found
370 for cases with $d_n = 0.015625$ mm and $2 \times 10^{-3} < Re_p < 3 \times 10^{-3}$, and so are not included
371 here.

372 Taking ellipsoid 1 as an example, Fig. 6 shows the temporal variations in orientation
373 angle β , settling velocity W , and vertical displacement s . It can be seen that β
374 remains constant during the settling process for cases with different β_0 [Fig. 6(a)]. This
375 suggests that the orientation remains essentially unchanged for non-spherical particles
376 settling in the Stokes regime, in agreement with previous findings.^{27,28} As a result, a non-
377 spherical particle reaches a terminal velocity that depends on the initial orientation of the
378 particle [Fig. 6(b)]. And particles with larger β_0 tend to settle faster, yielding longer
379 vertical displacements [Fig. 6(c)].

380 To account for the effect of particle orientation, we consider crosswise sphericity ϕ_c ,
381 which is the ratio between the cross-sectional area of a volume-equivalent sphere and the
382 projection area of the actual particle perpendicular to the flow.¹⁶ According to the
383 definition of β , particles with large β should have relatively small projection areas
384 and consequently develop large ϕ_c .

385 Figure 7 illustrates the influence of particle orientation on terminal settling state by
386 showing the resulting variations in terminal velocity W_t and drag ratio F_{fd} / F_{pd} with
387 ϕ_c . In general, larger ϕ_c leads to larger W_t , indicating that the particle experiences

388 lower total drag at larger β . In addition, F_{fd} / F_{pd} tends to increase as ϕ_c increases,
 389 implying that the contribution from friction drag may increase despite reduction in total
 390 drag when the particle is oriented away from $\beta = 0^\circ$. Figure 8 presents contour plots of
 391 vertical flow velocity in the vicinity of particles of different shapes and initial orientation
 392 $\beta_0 = 45^\circ$ at the terminal settling state. Cases with $\beta_0 = 45^\circ$ are of particular interest
 393 because the particles display asymmetric forms in the vertical plane. As shown in Fig. 8,
 394 the velocity contours exhibit a highly symmetric pattern and turn out to be similar for
 395 different particle shapes. The particles seem to move in combination with the surrounding
 396 fluid, and so the effect of asymmetry of the solid shape is marginal. Arguably, this
 397 accounts for the sustainability of random orientations.

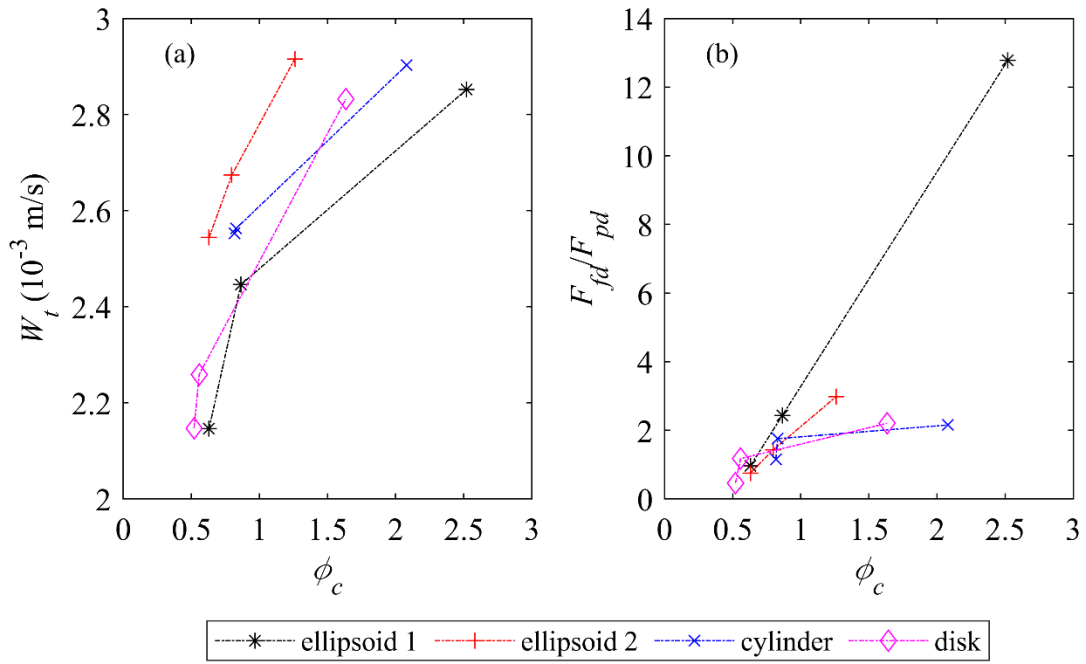


398

399 **FIG. 6.** Time histories of (a) orientation angle β , (b) settling velocity W , and (c)

400 vertical displacement s for ellipsoid 1 with $d_n = 0.0625$ mm .

401

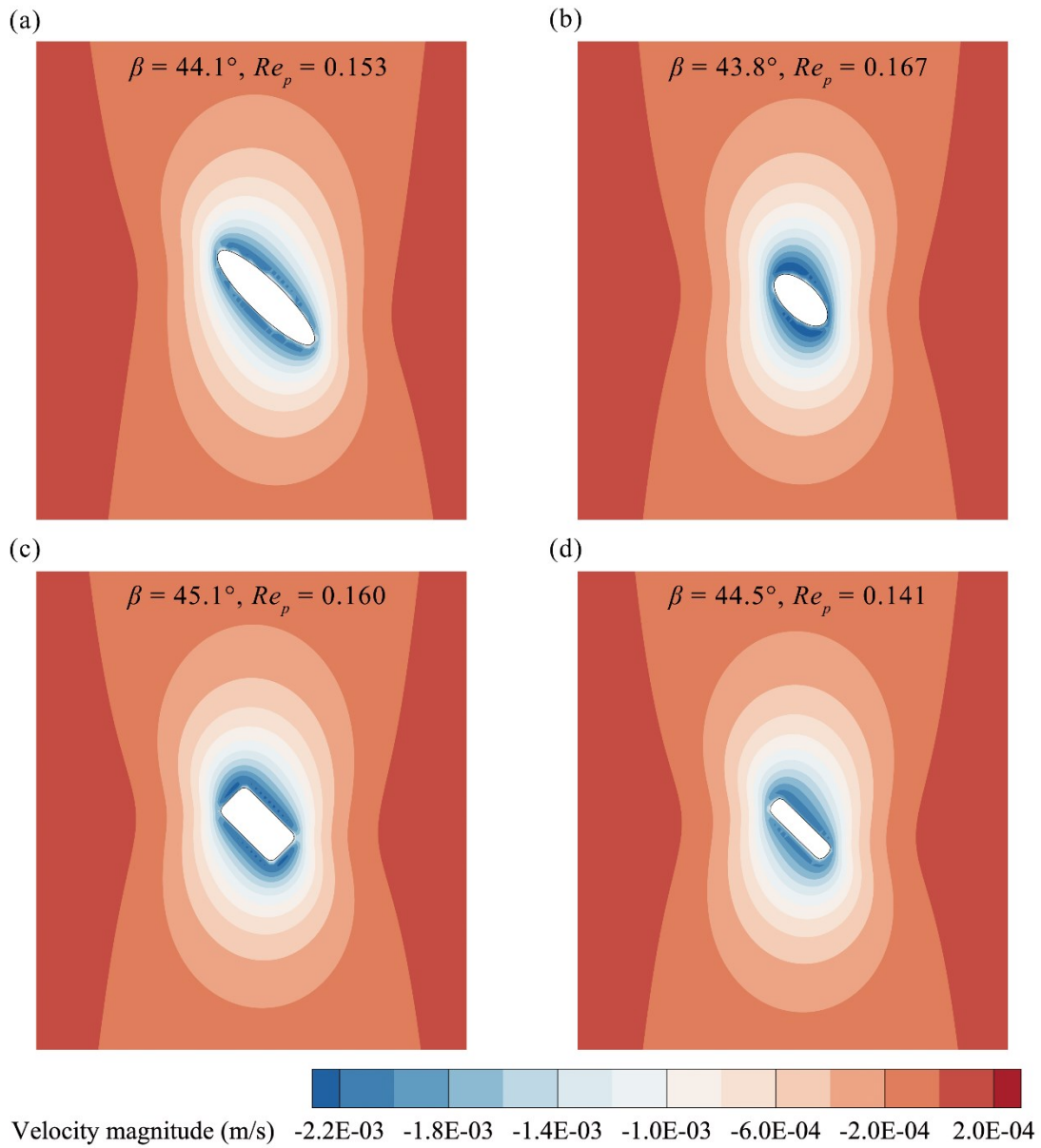


402

403 **FIG. 7.** Predicted dependencies of (a) terminal velocity W_t and (b) drag ratio F_{fd}/F_{pd}

404 on crosswise sphericity ϕ_c for particles of different shapes with $d_n = 0.0625$ mm .

405



406

407 **FIG. 8.** Contour plots of vertical flow velocity around differently shaped particles with
 408 $d_n = 0.0625$ mm and $\beta_0 = 45^\circ$ at the terminal settling state ($t = 0.06$ s): (a) ellipsoid 1,
 409 (b) ellipsoid 2, (c) cylinder, and (d) disk.

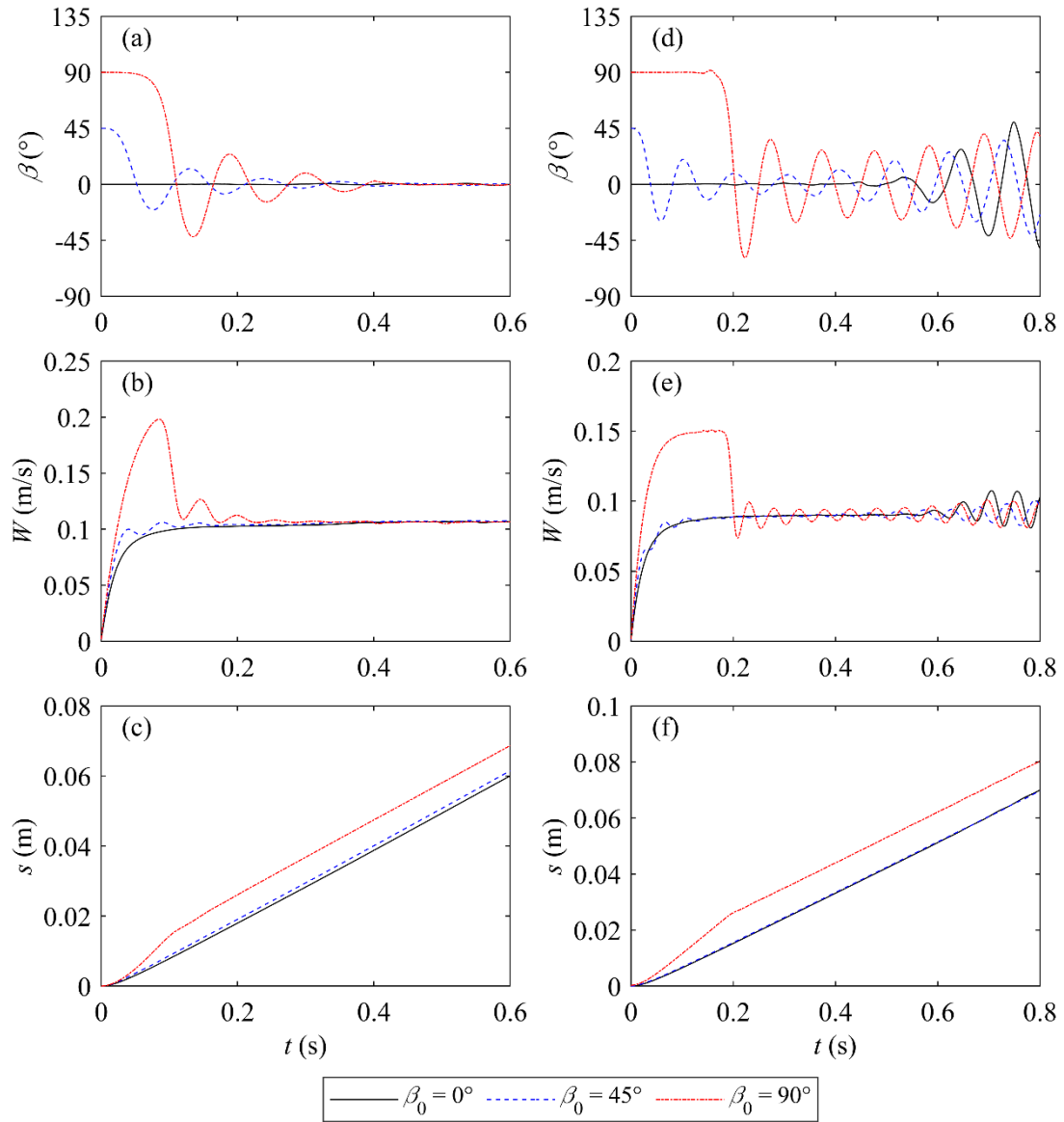
410

411 2. *Intermediate regime*

412 Here numerical cases with $d_n = 1$ mm and $Re_p \approx 100$ are selected to probe into
413 the effect of initial orientation on the settling of non-spherical particles in the intermediate
414 regime. As can be seen from Fig. 9(a), particles of ellipsoid 1 shape tend to attain the
415 same terminal settling state with $\beta = 0^\circ$ irrespective of their initial orientation,
416 consistent with the previously mentioned settling behavior at relatively large Re_p .^{8,29}
417 Variation in particle orientation has a vital effect on the settling process, about which more
418 details are given later in this section. Yet, due to the identical orientation attained at
419 terminal settling, the effect of initial orientation on terminal velocity can be negligible
420 [see Fig. 9(b)]. Except for the disk, similar results have been found for other particle
421 shapes. At the terminal settling state, periodic oscillations about $\beta = 0^\circ$ are observed
422 for the disk particle [Figs. 9(d) and 9(e)]. Such results are in accordance with previous
423 observations by Stringham et al.⁴⁷ at a higher value of Re_p .

424 Fig. 10 depicts two-dimensional visualizations of the settling trajectory and
425 orientation variation of different particles with $\beta_0 = 90^\circ$. The red dashed line denotes the
426 centroid trajectory and the black solid line with blue endpoints denotes the location of the
427 revolution axis. The time increment between each visualization is 0.02 s. During the
428 settling process, the revolution axes of elongated particles (ellipsoid 1 and the cylinder)
429 become gradually oriented normal to the direction of settling motion, while those of flat
430 particles (ellipsoid 2 and the disk) turn to be parallel to the settling direction, thus the
431 $\beta = 0^\circ$ state is eventually reached. In addition to the vertical fall, a horizontal component
432 can be observed in the settling path, associated with the varying orientation.

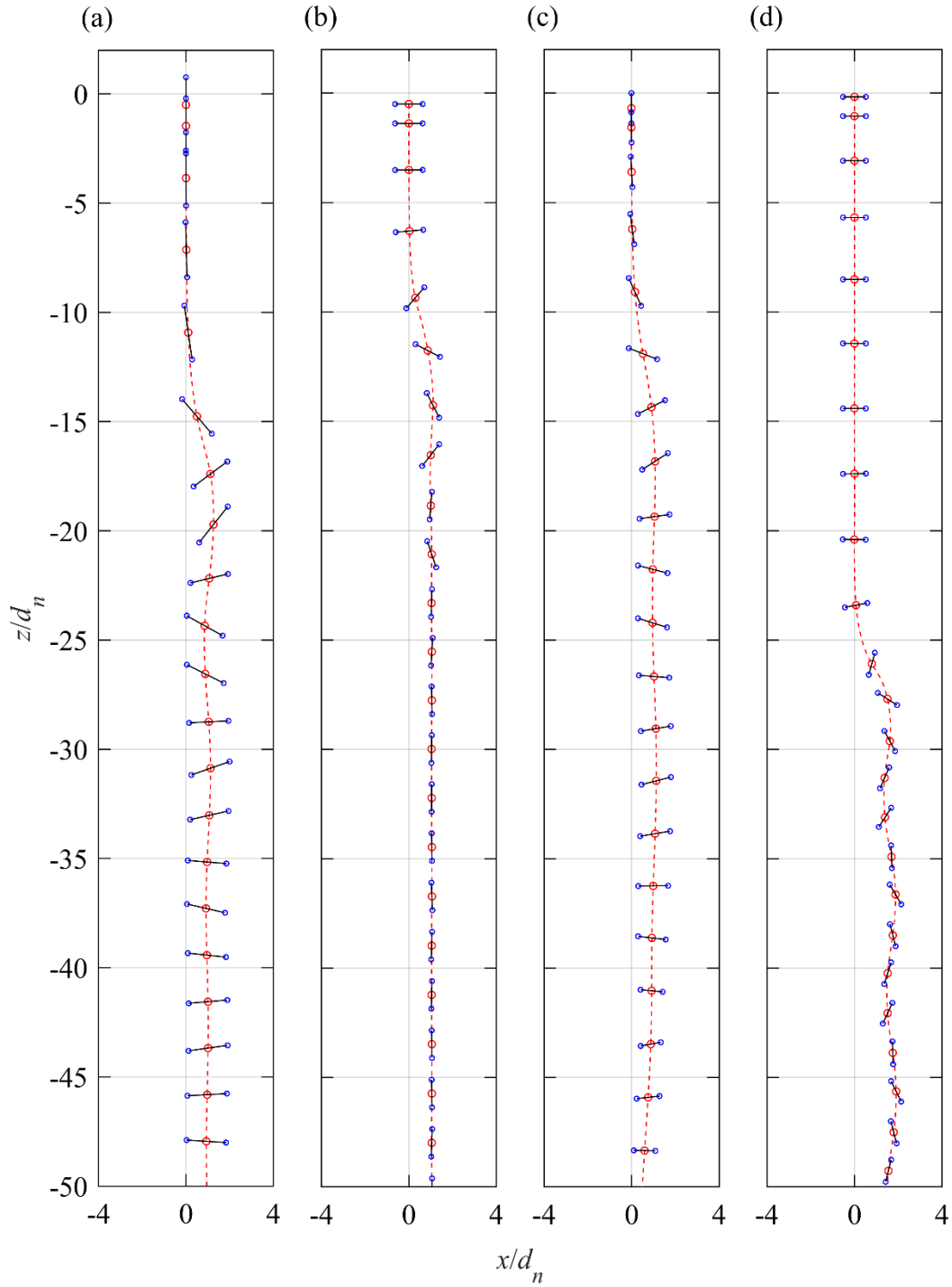
433



434

435 **FIG. 9.** Time histories of orientation angle β , settling velocity W , and vertical
 436 displacement s for (a-c) ellipsoid 1 and (d-f) disk with $d_n = 1$ mm.

437



438

439 **FIG. 10.** Variations in settling trajectory and orientation of different particles with
 440 $d_n = 1 \text{ mm}$, $\beta_0 = 90^\circ$ and shape: (a) ellipsoid 1, (b) ellipsoid 2, (c) cylinder, and (d) disk.

441 Red dashed line denotes the centroid trajectory, and black solid line with blue endpoints
 442 denotes the location of the revolution axis. The lengths of the revolution axes of ellipsoid
 443 2 and the disk are doubled and tripled respectively for clarity. The time increment between
 444 each visualization is 0.02 s.

445 Given that gravitational force induces no torque about the mass center, torque arising
446 from hydrodynamic forces is responsible for particle rotation. According to Mandø and
447 Rosendahl⁸, friction torque always acts to damp rotational motion, whereas torque
448 stemming from the offset of the center of pressure from the geometric center (i.e., the
449 mass center) accounts for particle readjustment. Figure 11 illustrates the pressure
450 distribution around ellipsoid 1 at different instants of settling for $\beta_0 = 90^\circ$. During the
451 initial period, the particle moves at its initial orientation (i.e., $\beta = \beta_0 = 90^\circ$) [Fig. 11(a)].
452 Although the particle experiences no torque under such circumstances, this can
453 instinctively be interpreted as a state of unstable equilibrium. Once it experiences a certain
454 level of disturbance, the particle starts to deviate from the state of unstable equilibrium,
455 and the pressure distribution is no longer symmetric around the particle [Figs. 11(b) and
456 11(c)]. This change promotes additional torque due to the displacement of the center of
457 pressure, thus forcing the particle to rotate. Eventually, a state of stable equilibrium is
458 reached whereby the center of pressure is consistent with the geometric center, and the
459 torque vanishes [Fig. 11(d)]. The terminal settling state of a particle is commonly
460 characterized by this stable equilibrium state without regard to secondary motions like
461 oscillation.

462 Based on the above description, the settling process of a non-spherical particle in the
463 intermediate regime may be divided into three chronological stages. In Stage 1, the
464 particle provisionally settles at an unstable equilibrium state. In Stage 2, the particle self-
465 readjusts to the stable equilibrium state. In Stage 3, the particle progressively attains the
466 terminal settling state where secondary motions may occur. Notably, particles with certain
467 initial orientations may not experience Stage 1 and even Stage 2. Moreover, the settling
468 velocity can dramatically increase in Stage 1, leading to a considerably longer vertical

469 displacement [see Figs. 9(c) and 9(f)]. Particles with $d_n = 0.25$ mm ($Re_p \approx 10$) exhibit
470 qualitatively similar settling behavior to those with $d_n = 1$ mm, yet appear to be oriented
471 directly to the stable equilibrium state of $\beta = 0^\circ$ without exhibiting oscillations in Stage
472 2 (Fig. 12).

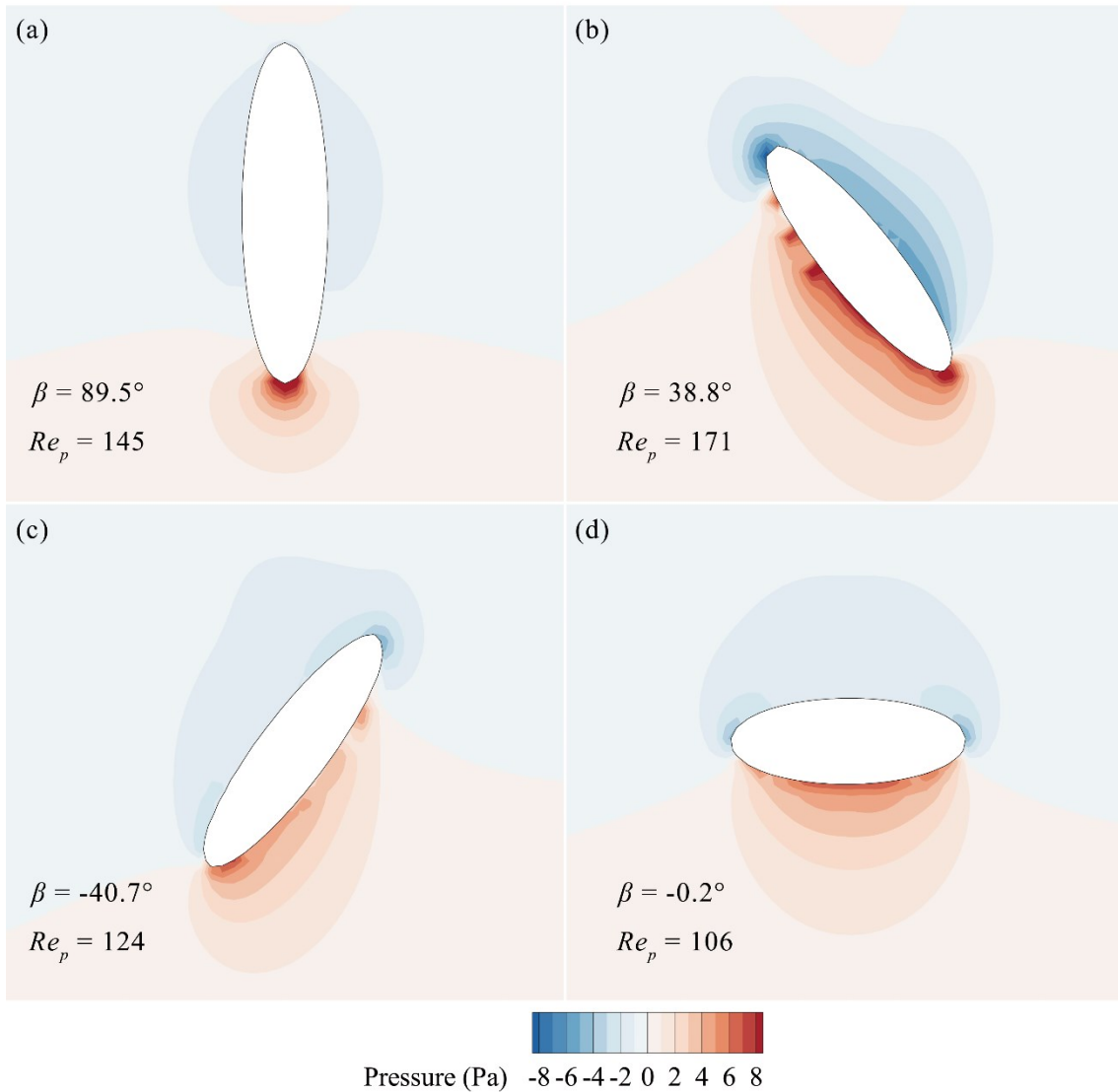
473 As a settling particle rotates due to hydrodynamic torque, the rotational motion of
474 the particle can in turn appreciably affect the flow field around it and may thus promote
475 specific wake structures. Fig. 13 visualizes the flow fields around particles of different
476 shapes with $d_n = 1$ mm and $\beta_0 = 90^\circ$. The Ω_R method proposed by Dong et al.⁴⁸ is
477 used for vortex identification. An iso-surface of $\Omega_R = 0.52$ is chosen to capture the
478 vortical structures. As illustrated in Fig. 13(a), the wake of ellipsoid 1 initially consists of
479 two thread-like vortices that are attached to the particle. As the particle rotates, instability
480 develops, and vortex shedding occurs. The detaching vortices push the flow near and
481 around the particle upwards, forming a low-pressure region that generates a torque on the
482 particle in the opposite direction. This additional torque along with inertia can further lead
483 to particle oscillations because new vortices can detach on the other side when the particle
484 reaches the opposite inclination and so on, each time it changes orientation. Notably, the
485 vortical structure is closely related to the particle shape. Similar to ellipsoid 1, a double-
486 threaded wake structure is observed for the cylinder [Fig. 13(c)], whereas flatter particles
487 like ellipsoid 2 and the disk present a so-called hairpin structure^{49,50} [Figs. 13(b) and
488 13(d)]. Vortex shedding is less pronounced for particles with $d_n = 1$ mm and $\beta_0 = 45^\circ$.
489 This is mainly because the absence of Stage 1 leads to relatively low Re_p in Stage 2.
490 For particles with $d_n = 0.25$ mm however, no vortex shedding is observed for all
491 simulated shapes and initial orientations. The foregoing suggests that the occurrence of

492 vortex shedding depends largely on the magnitude of Re_p . An unstable initial orientation
493 may promote vortex shedding because larger Re_p can be reached and rotational motion
494 is induced. In turn, vortex shedding can affect the settling motion by causing the particle
495 to oscillate in Stage 2 and Stage 3.

496 Figure 14 presents contour plots of the vertical flow velocity component around
497 particles of different shapes for $d_n = 1$ mm and $\beta_0 = 90^\circ$. Sinuous wake structures
498 associated with varying particle orientation can be observed. Moreover, the velocity
499 distribution in the wake exhibits an asymmetric pattern even as the particle approaches
500 the state of stable equilibrium [Figs. 14(a) and 14(d)]. In fact, the high-velocity zone is
501 located close to the downward-rotating end of the particle, reflecting the effect of
502 rotational motion on the flow field.

503 Overall, our results provide insight into the settling process of non-spherical particles
504 in the intermediate regime. The initial orientation of non-spherical particles plays a key
505 role in the settling process and so should be taken into account for particulate flows.

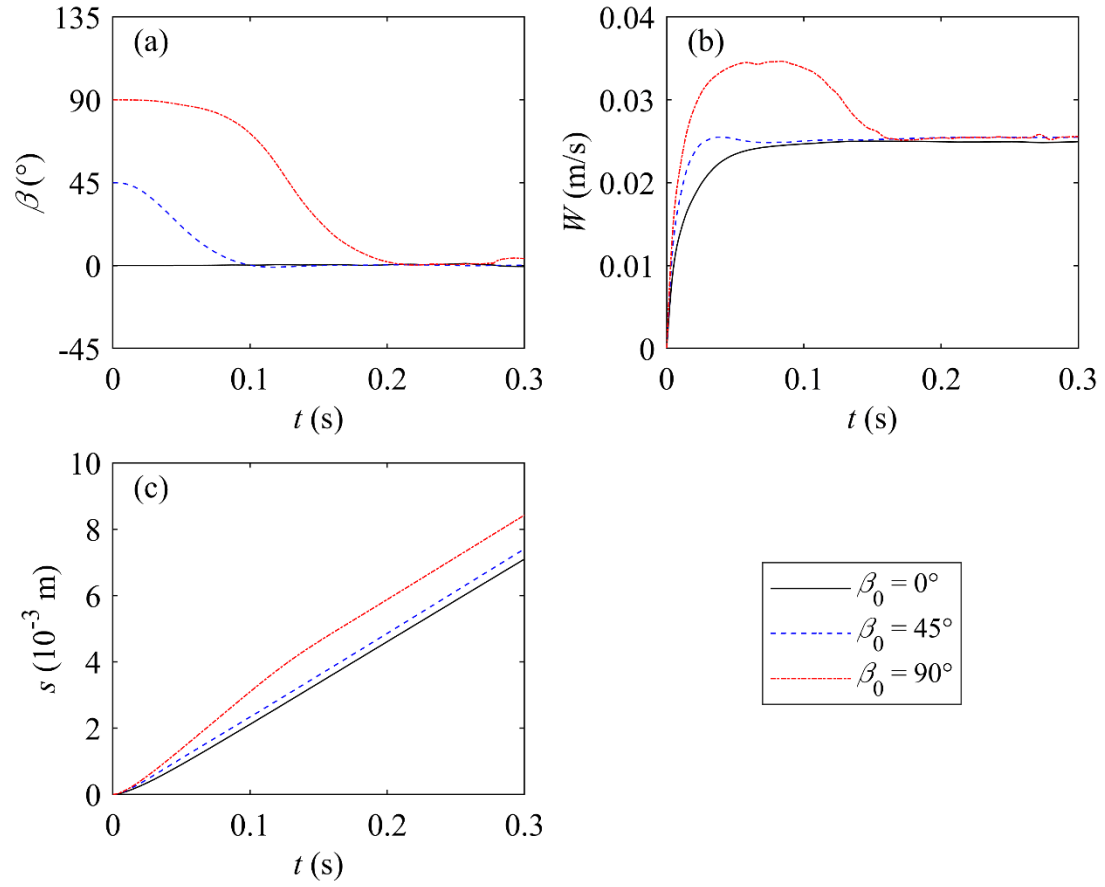
506



507

508 **FIG. 11.** Pressure distribution contours around ellipsoid 1 with $d_n = 1$ mm and
 509 $\beta_0 = 90^\circ$ at different instants of settling: $t =$ (a) 0.04 s, (b) 0.10 s, (c) 0.14 s, and (d)
 510 0.60 s.

511

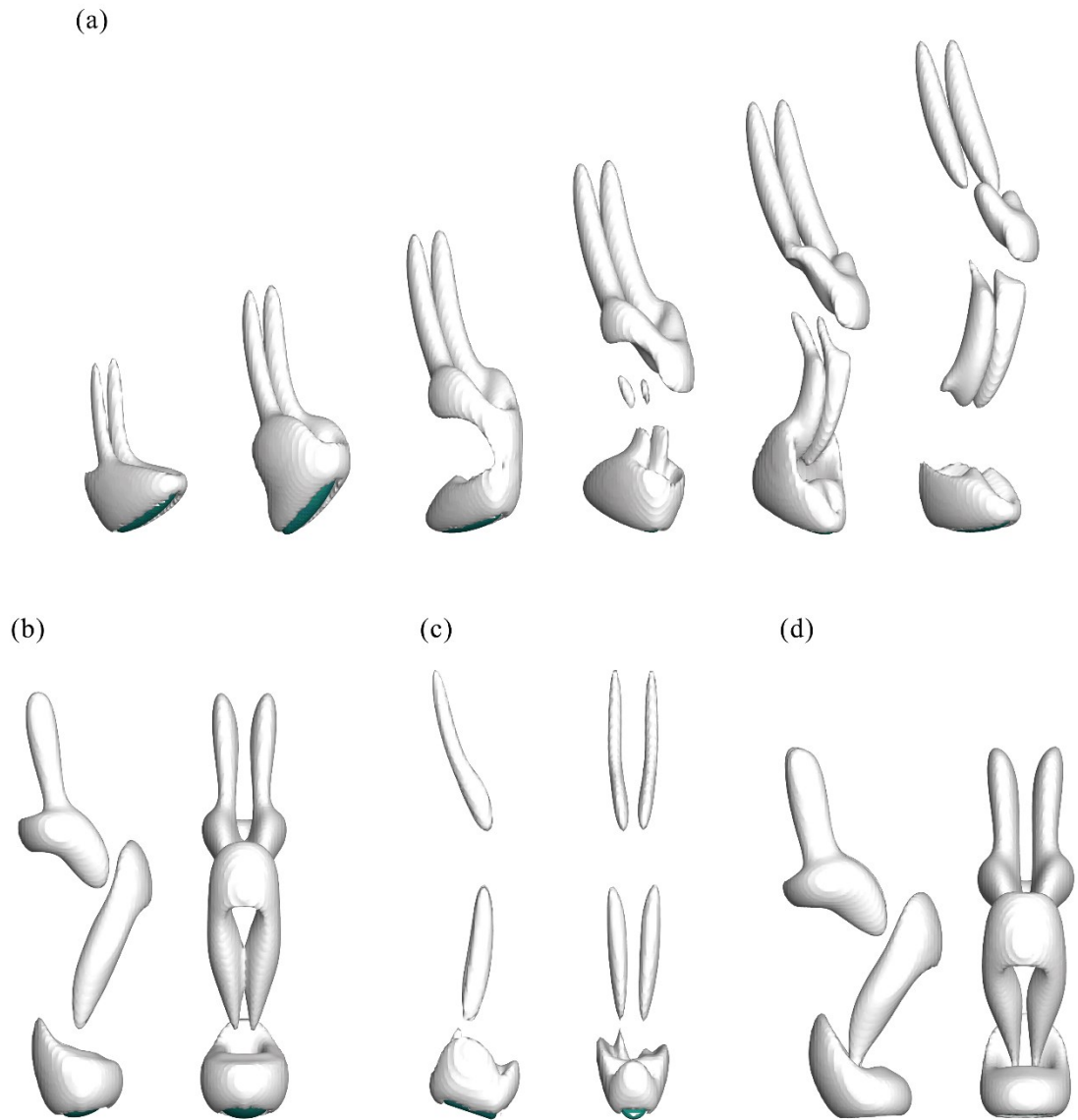


512

513 **FIG. 12.** Time histories of (a) orientation angle β , (b) settling velocity W , and (c)

514 vertical displacement s for ellipsoid 1 with $d_n = 0.25$ mm .

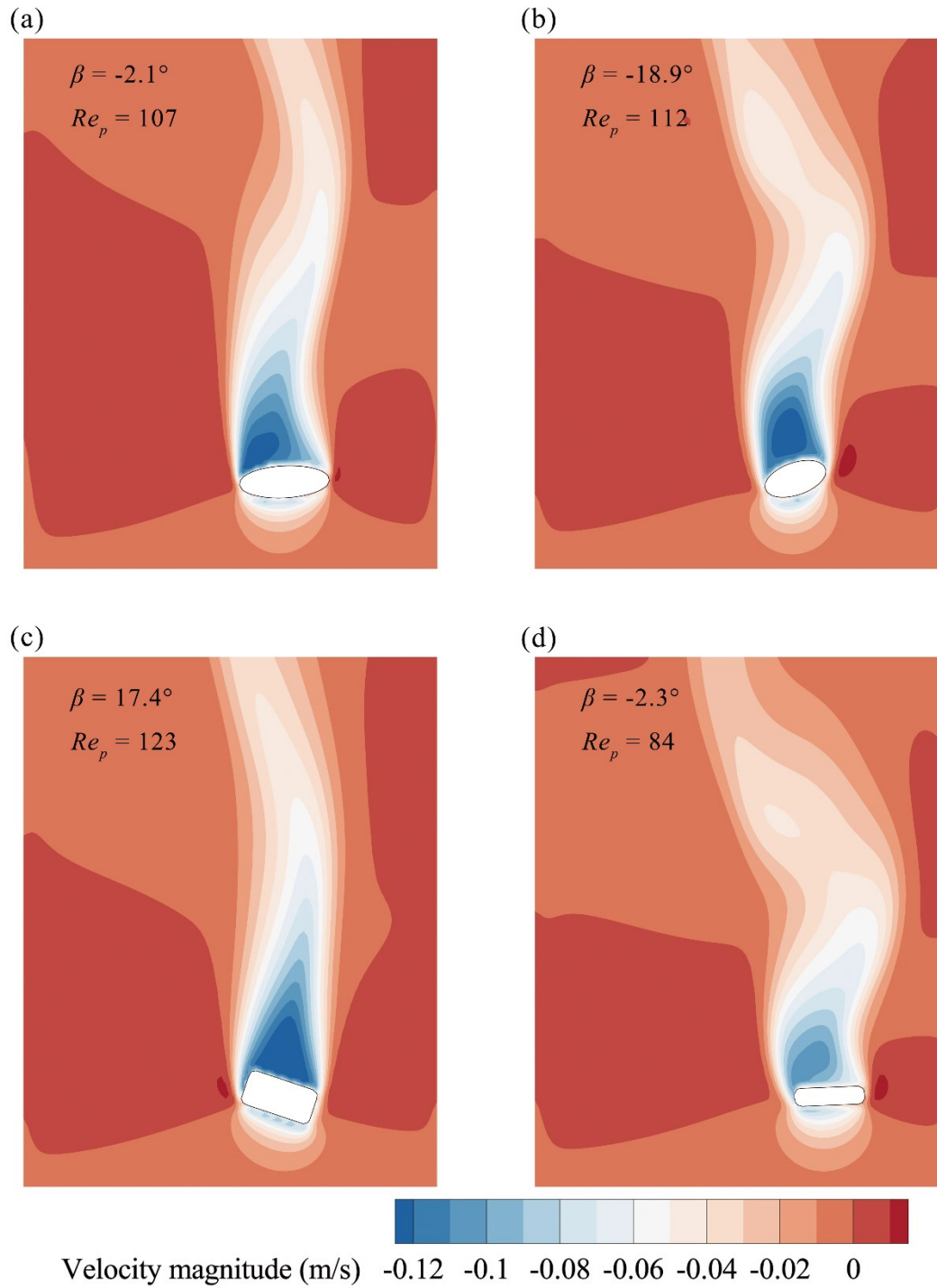
515



516

517 **FIG. 13.** Vortices in the wake of particles of different shapes for $d_n = 1$ mm and
 518 $\beta_0 = 90^\circ$ during orientation readjustment: (a) ellipsoid 1, $t = 0.12\sim 0.22$ s, (b) ellipsoid 2,
 519 $t = 0.18$ s, (c) cylinder, $t = 0.20$ s, and (d) disk, $t = 0.30$ s. An iso-surface of $\Omega_r = 0.52$
 520 is chosen to capture vortical structures.⁴⁸

521



522

523 **FIG. 14.** Contour plots of vertical flow velocity component around particles of different
 524 shapes with $d_n = 1$ mm and $\beta_0 = 90^\circ$ during orientation readjustment: (a) ellipsoid 1,
 525 $t = 0.22$ s, (b) ellipsoid 2, $t = 0.18$ s, (c) cylinder, $t = 0.20$ s, and (d) disk, $t = 0.30$ s .

526

527 IV. CONCLUSION

528 This study has investigated the effects of particle shape and initial orientation on the
529 settling of non-spherical particles. Commercial CFD software FLOW-3D was used to
530 perform a series of PR-DNS simulations of the settling in otherwise quiescent water of
531 spheres and five types of regular, non-spherical sediment particles, i.e., prolate spheroid,
532 oblate spheroid, cylinder, disk, and cube. A dual-Euler whole-attitude solver was used to
533 reproduce particle orientation behavior. In the study, the Galileo number was varied from
534 0.248 to 360 with the particle Reynolds number Re_p ranging from 0.00277 to 562.
535 Based on the computational results, the main findings are summarized as follows:

536 (1) A non-spherical particle experiences larger drag and consequently attains a lower
537 terminal velocity than its spherical counterpart. For sufficiently small Re_p
538 when the viscous force dominates, the terminal velocity is less affected by the
539 particle shape (characterized by the particle aspect ratio). For relatively large
540 Re_p when the inertial force becomes dominant, the shape effect becomes
541 significant, and should be represented by the Corey shape factor. When the
542 inertial force becomes significant or the particle shape deviates from a sphere,
543 then pressure drag may dominate over friction drag.

544 (2) Empirical correlations were derived for the dimensionless characteristic time
545 t_{95^*} and dimensionless characteristic displacement s_{95^*} of particle settling. It
546 was demonstrated that t_{95^*} remains constant in the Stokes regime and decreases
547 as Re_p increases in the intermediate regime; s_{95^*} increases logarithmically
548 with increasing Re_p over the simulated range, whereas the slope in s_{95^*} with

549 Re_p observed in the Stokes regime reduces in the intermediate regime.

550 (3) In the Stokes regime, the orientation of a non-spherical particle remains
551 essentially unchanged during the settling process. A non-spherical particle with
552 different initial orientations can attain various terminal velocities which increase
553 with crosswise sphericity ϕ_c . The flow velocity distribution in the vicinity of a
554 particle of any shape exhibits a highly symmetric pattern. A given particle
555 appears to move in tandem with the surrounding fluid, such that the effect of its
556 asymmetry is marginal.

557 (4) In the intermediate regime, a non-spherical particle provisionally settling at an
558 unstable orientation tends to readjust itself to a stable equilibrium state. In
559 general, such a particle may experience three stages during its settling process:
560 settling provisionally at an unstable equilibrium state; self-readjusting to the
561 stable equilibrium state; and progressively approaching the terminal state where
562 secondary motions may occur. Due to the identical orientation attained at
563 terminal settling, the effect of initial orientation on terminal velocity is negligible,
564 while an unstable initial orientation can result in a longer vertical displacement
565 and may promote vortex shedding. It is therefore important to consider the initial
566 orientation of non-spherical particles when modeling particulate flows.

567 In many real-world situations, particles do not settle in isolation. Vortices induced by
568 nearby particles can significantly influence the overall settling behavior, e.g., causing
569 repulsion in dual-particle cases,⁵¹ promoting clusters for monodisperse particles,⁵² and
570 altering the orientation of rod-like particles.⁵³ Direct inter-particle interactions (collisions)
571 also play an important role in the dynamics of particles particularly when in a dense
572 regime.^{54,55} Therefore, we intend to carry out future research into the behavior of multi-

573 particle systems. Moreover, the present work has provided us with a unique basis to
574 investigate the settling of irregular particles; this work is underway.

575

576 SUPPLEMENTARY MATERIAL

577 The Supplementary Material provides a brief description of the dual-Euler whole-
578 attitude solver used to model variation in particle orientation.

579

580 ACKNOWLEDGMENTS

581 The present work was financially supported by the National Natural Science
582 Foundation of China (Grant No. 52239007).

583

584 AUTHOR DECLARATIONS

585 Conflict of Interest

586 The authors have no conflicts to disclose.

587

588 Author Contributions

589 **Xiaoyong Cheng:** Data curation (lead); Formal analysis (lead); Investigation (equal);
590 Methodology (equal); Validation (lead); Visualization (lead); Writing – original draft
591 (lead). **Zhixian Cao:** Conceptualization (equal); Funding acquisition (lead); Investigation
592 (equal); Methodology (equal); Project administration (lead); Resources (lead);

593 Supervision (lead); Writing – review & editing (equal). **Ji Li**: Conceptualization (equal);
594 Investigation (equal); Writing – review & editing (equal). **Alistair Borthwick**:
595 Conceptualization (equal); Investigation (equal); Writing – review & editing (equal).

596

597 DATA AVAILABILITY

598 Data that support the findings of this study are available from the corresponding
599 author upon reasonable request.

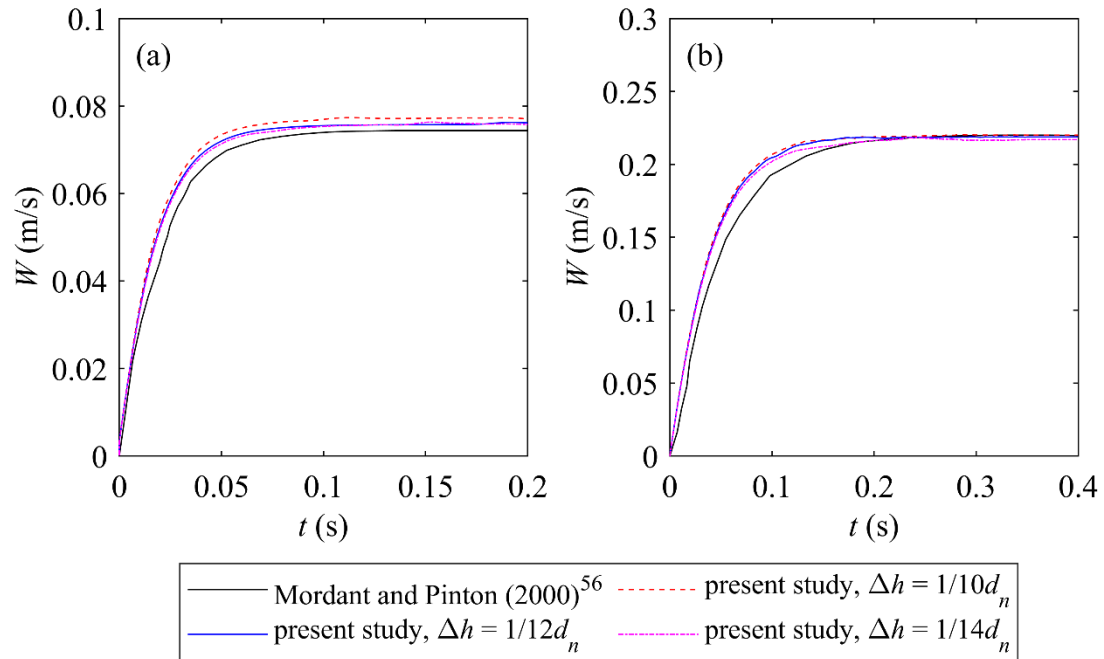
600

601 APPENDIX: VALIDATION OF THE CFD MODEL

602 The settling of a solid sphere in quiescent water was experimentally investigated by
603 Mordant and Pinton⁵⁶ who derived the temporal variation in settling velocity from
604 measurements of the Doppler shift of an ultrasonic wave scattered by a moving particle.
605 Two cases with $d_n = 0.5$ mm and 1.5 mm are simulated to validate the applied CFD
606 model. The particle density is $\rho_p = 2560$ kg/m³, the water density is $\rho_f = 1000$ kg/m³,
607 and the dynamic viscosity of water $\mu = 8.9 \times 10^{-4}$ kg/m/s. The simulation setup is the
608 same as previously described in Sec. II.B except that three mesh resolutions are tested,
609 i.e., $\Delta h = 1/10$, $1/12$, and $1/14 d_n$.

610 Fig. 15 shows that there is good agreement between the simulated and measured
611 settling velocities, thus validating the model, and demonstrating that a mesh resolution of
612 $\Delta h = 1/12 d_n$ is sufficiently fine to produce accurate results.

613



614

615 **FIG. 15.** Time history of settling velocity W for spheres of (a) $d_n = 0.5$ mm and (b)
 616 $d_n = 1.5$ mm. Black solid line refers to measured data by Mordant and Pinton⁵⁶.

617

618 REFERENCES

619 ¹M. Church, “Bed material transport and the morphology of alluvial river channels,”
 620 *Annu. Rev. Earth Planet. Sci.* **34**(1), 325-354 (2006).

621 ²S. Dey, A. S. Zeeshan, and E. Padhi, “Terminal fall velocity: the legacy of Stokes from
 622 the perspective of fluvial hydraulics,” *Proceedings of the Royal Society A* **475**(2228),
 623 20190277 (2019).

624 ³I. A. Kane and M. A. Clare, “Dispersion, accumulation, and the ultimate fate of
 625 microplastics in deep-marine environments: A review and future directions,” *Front. Earth*
 626 *Sci.* **7**, 00080 (2019).

627 ⁴J. Li, E. Shan, J. Zhao, J. Teng, and Q. Wang, “The factors influencing the vertical
 628 transport of microplastics in marine environment: A review,” *Sci. Total Environ.* **870**,

629 161893 (2023).

630 ⁵B. R. Barboza, B. Chen, and C. Li, “A review on proppant transport modelling,” *J. Pet.*
631 *Sci. Eng.* **204**, 108753 (2021).

632 ⁶S. Yao, C. Chang, K. Hai, H. Huang, and H. Li, “A review of experimental studies on the
633 proppant settling in hydraulic fractures,” *J. Pet. Sci. Eng.* **208**, 109211 (2022).

634 ⁷R. P. Chhabra and J. F. Richardson, *Non-Newtonian Flow and Applied Rheology:*
635 *Engineering Applications* (Butterworth-Heinemann, 2008).

636 ⁸M. Mandø and L. Rosendahl, “On the motion of non-spherical particles at high Reynolds
637 number,” *Powder Technol.* **202**, 1-13 (2010).

638 ⁹H. Ma, L. Zhou, Z. Liu, M. Chen, X. Xia, and Y. Zhao, “A review of recent development
639 for the CFD-DEM investigations of non-spherical particles,” *Powder Technol.* **412**,
640 117972 (2022).

641 ¹⁰Y. Zhao, P. Zhang, L. Lei, L. Kong, S. A. Galindo-Torres, and S. Z. Li, “Metaball-
642 Imaging discrete element lattice Boltzmann method for fluid–particle system of complex
643 morphologies with case studies,” *Phys. Fluids* **35**(2), 023308 (2023).

644 ¹¹R. Clift and W. H. Gauvin, “Motion of entrained particles in gas streams,” *Can. J. Chem.*
645 *Eng.* **49**(4), 439-448 (1971).

646 ¹²N. Cheng, “Comparison of formulas for drag coefficient and settling velocity of
647 spherical particles,” *Powder Technol.* **189**(3), 395-398 (2009).

648 ¹³A. Terfous, A. Hazzab, and A. Ghenaim, “Predicting the drag coefficient and settling
649 velocity of spherical particles,” *Powder Technol.* **239**, 12-20 (2013).

650 ¹⁴W. E. Dietrich, “Settling velocity of natural particles,” *Water Resour. Res.* **18**(6), 1615-
651 1626 (1982).

652 ¹⁵A. Haider and O. Levenspiel, “Drag coefficient and terminal velocity of spherical and
653 nonspherical particles,” *Powder Technol.* **58**(1), 63-70 (1989).

654 ¹⁶A. Hölzer and M. Sommerfeld, “New simple correlation formula for the drag coefficient
655 of non-spherical particles,” *Powder Technol.* **184**(3), 361-365 (2008).

656 ¹⁷F. Dioguardi and D. Mele, “A new shape dependent drag correlation formula for non-
657 spherical rough particles. Experiments and results,” *Powder Technol.* **277**, 222-230
658 (2015).

659 ¹⁸G. Bagheri and C. Bonadonna, “On the drag of freely falling non-spherical particles,”
660 *Powder Technol.* **301**, 526-544 (2016).

661 ¹⁹A. T. Corey, “Influence of shape on the fall velocity of sand grains,” Ph.D. thesis
662 (Colorado State University, 1949).

663 ²⁰B. J. Connolly, E. Loth, and C. F. Smith, “Shape and drag of irregular angular particles
664 and test dust,” *Powder Technol.* **363**, 275-285 (2020).

665 ²¹Y. Li, Q. Yu, S. Gao, and B. W. Flemming, “Settling velocity and drag coefficient of
666 platy shell fragments,” *Sedimentology* **67**(4), 2095-2110 (2020).

667 ²²S. Chien, “Settling velocity of irregularly shaped particles,” *SPE Drill. Complet.* **9**(04),
668 281-289 (1994).

669 ²³X. Song, Z. Xu, G. Li, Z. Pang, and Z. Zhu, “A new model for predicting drag coefficient
670 and settling velocity of spherical and non-spherical particle in Newtonian fluid,” *Powder*
671 *Technol.* **321**, 242-250 (2017).

672 ²⁴R. Büttner, P. Dellino, L. La Volpe, V. Lorenz, and B. Zimanowski, “Thermohydraulic
673 explosions in phreatomagmatic eruptions as evidenced by the comparison between
674 pyroclasts and products from Molten Fuel Coolant Interaction experiments,” *Journal of*
675 *Geophysical Research: Solid Earth* **107**(B11), ECV 5-1-ECV 5-14 (2002).

676 ²⁵P. Dellino, D. Mele, R. Bonasia, G. Braia, L. La Volpe, and R. Sulpizio, “The analysis
677 of the influence of pumice shape on its terminal velocity,” *Geophys. Res. Lett.* **32**(21)
678 (2005).

679 ²⁶Y. Wang, L. Zhou, Y. Wu, and Q. Yang, “New simple correlation formula for the drag
680 coefficient of calcareous sand particles of highly irregular shape,” *Powder Technol.* **326**,
681 379-392 (2018).

682 ²⁷R. Clift, J. R. Grace, and M. E. Weber, *Bubbles, Drops, and Particles* (Academic Press,
683 New York, 1978).

684 ²⁸E. Loth, “Drag of non-spherical solid particles of regular and irregular shape,” *Powder*
685 *Technol.* **182**(3), 342-353 (2008).

686 ²⁹M. de Kruijf, A. Sloodman, R. A. de Boer, and J. J. G. Reijmer, “On the settling of marine
687 carbonate grains: Review and challenges,” *Earth-Sci. Rev.* **217**, 103532 (2021).

688 ³⁰M. Zastawny, G. Mallouppas, F. Zhao, and B. van Wachem, “Derivation of drag and lift
689 force and torque coefficients for non-spherical particles in flows,” *Int. J. Multiph. Flow*
690 **39**, 227-239 (2012).

691 ³¹R. Ouchene, M. Khalij, B. Arcen, and A. Tanière, “A new set of correlations of drag, lift
692 and torque coefficients for non-spherical particles and large Reynolds numbers,” *Powder*
693 *Technol.* **303**, 33-43 (2016).

694 ³²S. K. P. Sanjeevi, J. A. M. Kuipers, and J. T. Padding, “Drag, lift and torque correlations
695 for non-spherical particles from Stokes limit to high Reynolds numbers,” *Int. J. Multiph.*
696 *Flow* **106**, 325-337 (2018).

697 ³³R. Ouchene, “Numerical simulation and modeling of the hydrodynamic forces and
698 torque acting on individual oblate spheroids,” *Phys. Fluids* **32**(7), 073303 (2020).

699 ³⁴F. Carranza and Y. Zhang, “Study of drag and orientation of regular particles using
700 stereo vision, Schlieren photography and digital image processing,” *Powder Technol.* **311**,
701 185-199 (2017).

702 ³⁵H. Başağaoğlu, S. Succi, D. Wyrick, and J. Blount, “Particle shape influences settling
703 and sorting behavior in microfluidic domains,” *Sci. Rep.* **8**(1) (2018).

704 ³⁶S. Ghosh and P. Yadav, “Study of gravitational settling of single semi-torus shaped
705 particle using immersed boundary method,” *Appl. Math. Comput.* **413**, 126643 (2022).

706 ³⁷D. Hui, Z. Xu, G. Zhang, and M. Liu, “Sedimentation of elliptical particles in Bingham
707 fluids using graphics processing unit accelerated immersed boundary-lattice Boltzmann
708 method,” *Phys. Fluids* **35**(1), 13330 (2023).

709 ³⁸C. W. Hirt and J. M. Sicilian, “A porosity technique for the definition of obstacles in
710 rectangular cell meshes,” in *International Conference on Numerical Ship Hydrodynamics*,
711 *4th*, Washington, DC (1985).

712 ³⁹F. Xiao, “A Computational Model for Suspended Large Rigid Bodies in 3D Unsteady
713 Viscous Flows,” *J. Comput. Phys.* **155**(2), 348-379 (1999).

714 ⁴⁰C. P. Tsai, Y. C. Chen, T. O. Sihombing, and C. Lin, “Simulations of moving effect of
715 coastal vegetation on tsunami damping,” *Nat. Hazards Earth Syst. Sci.* **17**(5), 693-702
716 (2017).

717 ⁴¹A. Kermanpur, S. Mahmoudi, and A. Hajipour, “Numerical simulation of metal flow
718 and solidification in the multi-cavity casting moulds of automotive components,” *J. Mater.*
719 *Process. Technol.* **206**(1-3), 62-68 (2008).

720 ⁴²X. Zhu, Y. H. Zeng, and W. X. Huai, “Settling velocity of non-spherical hydrochorous
721 seeds,” *Adv. Water Resour.* **103**, 99-107 (2017).

722 ⁴³G. H. Bagheri, C. Bonadonna, I. Manzella, and P. Vonlanthen, “On the characterization
723 of size and shape of irregular particles,” *Powder Technol.* **270**, 141-153 (2015).

724 ⁴⁴J. Guo, “Motion of spheres falling through fluids,” *J. Hydraul. Res.* **49**(1), 32-41 (2011).

725 ⁴⁵W. W. Rubey, “Settling velocity of gravel, sand, and silt particles,” *Am. J. Sci.* **s5-**
726 **25**(148), 325-338 (1933).

727 ⁴⁶J. Guo, “Logarithmic matching and its applications in computational hydraulics and
728 sediment transport,” *J. Hydraul. Res.* **40**(5), 555-565 (2002).

729 ⁴⁷G. E. Stringham, D. B. Simons, and H. P. Guy, *The Behavior of Large Particles Falling*
730 *in Quiescent Liquids* (US Government Printing Office, 1969).

731 ⁴⁸X. Dong, Y. Gao, and C. Liu, “New normalized Rortex/vortex identification method,”
732 *Phys. Fluids* **31**(1), 011701 (2019).

733 ⁴⁹H. Zhong, S. Chen, and C. Lee, “Experimental study of freely falling thin disks:
734 Transition from planar zigzag to spiral,” *Phys. Fluids* **23**(1), 011702 (2011).

735 ⁵⁰M. N. Ardekani, P. Costa, W. P. Breugem, and L. Brandt, “Numerical study of the
736 settling of spheroidal particles,” *Int. J. Multiph. Flow* **87**, 16-34 (2016).

737 ⁵¹J. Liu, P. Zhang, Y. Xiao, Z. Wang, S. Yuan, and H. Tang, “Interaction between dual
738 spherical particles during settling in fluid,” *Phys. Fluids* **33**(1), 013312 (2021).

739 ⁵²A. A. Zaidi, “Settling characteristics of bidisperse dilute suspension in the vortex
740 shedding regime,” *Phys. Fluids* **32**(9), 093310 (2020).

741 ⁵³A. Hamid, A. B. Arshad, S. Mehdi, M. D. Qasim, A. Ullah, J. J. Molina, and R.
742 Yamamoto, “A numerical study of sedimentation of rod like particles using smooth profile
743 method,” *Int. J. Multiph. Flow* **127**, 103263 (2020).

744 ⁵⁴A. Esteghamatian, A. Hammouti, M. Lance, and A. Wachs, “Particle resolved
745 simulations of liquid/solid and gas/solid fluidized beds,” *Phys. Fluids* **29**(3), 033302
746 (2017).

747 ⁵⁵Y. Yao, C. S. Criddle, and O. B. Fringer, “The effects of particle clustering on hindered
748 settling in high-concentration particle suspensions,” *J. Fluid Mech.* **920**, A40 (2021).

749 ⁵⁶N. Mordant and J. F. Pinton, “Velocity measurement of a settling sphere,” *Eur. Phys. J.*
750 *B* **18**(2), 343-352 (2000).

751